

## Article

# Neoproterozoic Mafic Magmatism in Nagercoil Block, Southern India and Its Implications on the Gondwana Collisional Orogeny

S. Sajna<sup>1,2</sup>, J. K. Tomson<sup>1,\*</sup>, J. Amal Dev<sup>1</sup> , Nilanjana Sorcar<sup>1</sup> and T. Vijaya Kumar<sup>3</sup><sup>1</sup> Solid Earth Research Group, National Centre for Earth Science Studies, Thiruvananthapuram 695011, India<sup>2</sup> Department of Marine Geology and Geophysics, Cochin University of Science and Technology (CUSAT), Kochi 682022, India<sup>3</sup> Council of Scientific and Industrial Research-National Geophysical Research Institute, Hyderabad 500007, India

\* Correspondence: Author: tomson.jk@ncss.gov.in

**Abstract:** The Nagercoil block situated at the southernmost tip of India occupies a key position in the East Gondwana collisional tectonic models. The Nagercoil block is dominated by Orosirian I-type charnockite massifs that host numerous gabbroic emplacements. Our present understanding about the crustal architecture of the Nagercoil block is derived mostly from these charnockites, while detailed studies on gabbros are lacking. We present new petrology, geochemistry, and zircon U-Pb/Hf isotopic data of gabbros from the Nagercoil block to understand their petrogenesis and tectonic significance. The results reveal that these are formed by the partial melting of a subduction-modified lithospheric mantle source in a continental arc setting. Zircon U-Pb geochronology results reveal that the gabbros were emplaced between 561 and 531 Ma. Hafnium isotopic studies on zircons argue for a mid-Mesoproterozoic melting source with near-juvenile magmatic signatures. The Hf-T<sub>DM</sub> ages together with the available data from the terrane point to the involvement of the adjacent Achankovil unit as a possible melting source contributor. The genetic link between the Achankovil unit and Sri Lanka together with the remarkable similarity in ages and isotopic characteristics of mafic rocks from both these terranes point to their coeval formation during the East African Orogeny associated with the final stages of the Gondwana supercontinent assembly.

**Keywords:** gabbro; zircon U-Pb/Hf geochronology; Southern Granulite Terrane; Nagercoil block



**Citation:** Sajna, S.; Tomson, J.K.; Dev, J.A.; Sorcar, N.; Kumar, T.V. Neoproterozoic Mafic Magmatism in Nagercoil Block, Southern India and Its Implications on the Gondwana Collisional Orogeny. *Minerals* **2022**, *12*, 1509. <https://doi.org/10.3390/min12121509>

Academic Editors: Alain Chauvet, Yonghong Shi, Fukun Chen and Jiahao Li

Received: 31 October 2022

Accepted: 23 November 2022

Published: 26 November 2022

**Publisher's Note:** MDPI stays neutral with regard to jurisdictional claims in published maps and institutional affiliations.



**Copyright:** © 2022 by the authors. Licensee MDPI, Basel, Switzerland. This article is an open access article distributed under the terms and conditions of the Creative Commons Attribution (CC BY) license (<https://creativecommons.org/licenses/by/4.0/>).

## 1. Introduction

The Precambrian granulitic terrane of southern India or the Southern Granulite Terrane (SGT) occupies a central position in the Gondwana supercontinent reconstruction models (Figure 1). This vast granulitic terrane has a crustal evolutionary history ranging from the early Archean to Cambrian with imprints of multiple magmatic, metamorphic, and deformation episodes [1–7]. In this protracted history, the Neoproterozoic assembly of SGT and its counterparts is known for high geotherm prevalence associated with intense crustal reworking and melting during the Himalayan-scale collision orogen referred to as the East African Orogen (EAO; 650–480 Ma; [5] and references therein). This collisional orogeny culminated in widespread HT-UHT metamorphism and the associated magmatism that affected vast tracts of the Precambrian crust in erstwhile Gondwana supercontinent fragments such as India, Sri Lanka, Madagascar, Antarctica, and Africa. Mafic magmatic rocks in these collisional belts are helpful for understanding crust–mantle processes responsible for their generation and their tectonic settings during the orogeny.

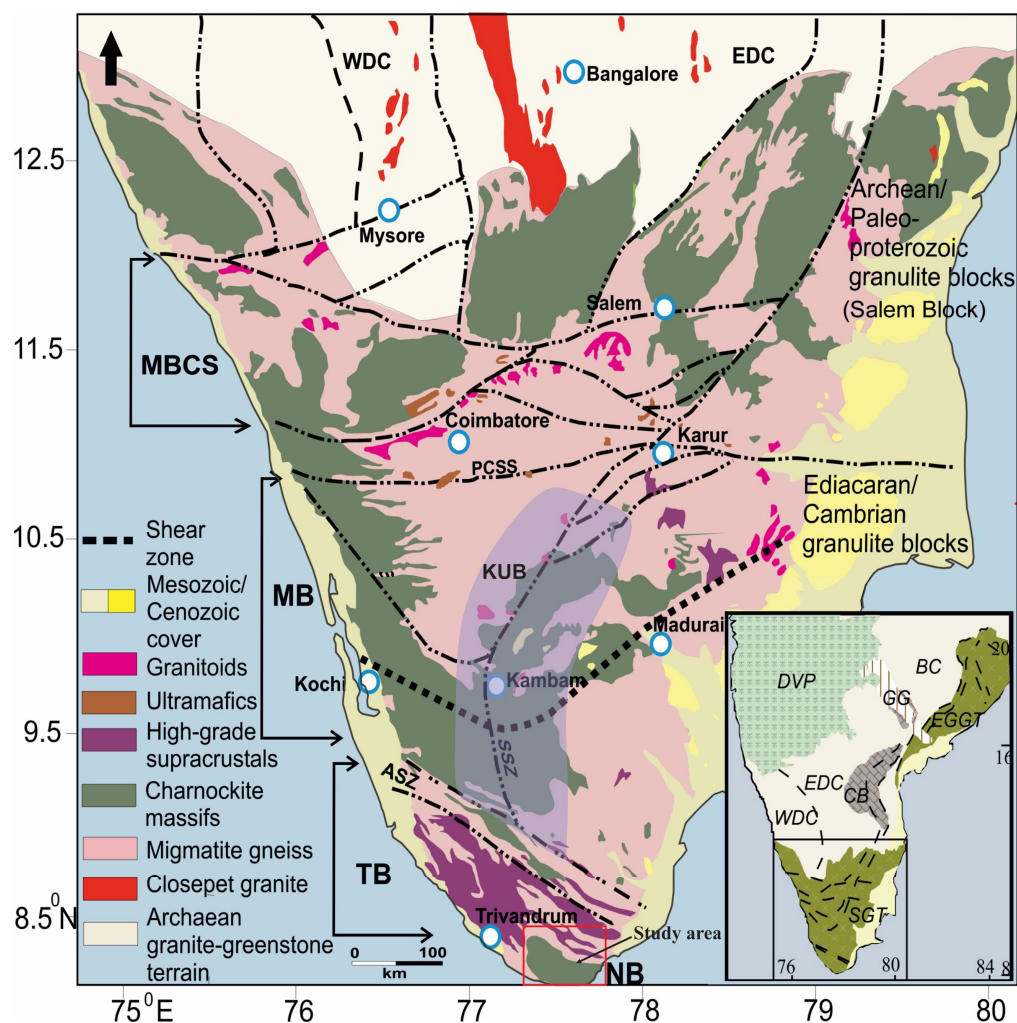


**Figure 1.** Simplified geological map of Southern Granulite Terrane (SGT; modified after [2]). Madurai block (MB), Trivandrum block (TB), Nagercoil block (NB), Western Dharwar Craton (WDC), Eastern Dharwar Craton (EDC), Moyar-Bhavani-Cauvery shear system (MBCS), Palghat-Cauvery shear system (PCSS), Suruli shear zone (SSZ), Karur-Kambam-Painavu-Trichur shear zone (KKPTSZ), Achankovil shear zone (ASZ), and Kambam UHT Belt (KUB). Inset shows the map of Indian peninsula: Deccan Volcanic Province (DVP), Bastar Craton (BC), Eastern Ghats Granulite Terrane (EGGT), Godaveri Graben (GG), and Cuddapah Basin (CB).

In SGT, though the mafic emplacements are reported in close spatial association with the HT-UHT granulites from all crustal blocks, less attention has been given to understanding their petrological, geochemical, and geochronological properties in detail. Collecting such information is vital to probe the genetic link between magmatism and metamorphism in the terrane and unravel its evolutionary history. The present study focuses on the mafic rocks reported from the southern tip of the SGT known as the Nagercoil block (Figure 2). We present new whole-rock geochemistry, mineral chemistry, and zircon U-Pb/Hf isotopic data of these rocks to understand their age and petrogenesis and to correlate with similar rocks from adjacent terranes within the SGT as well as from other Gondwanan fragments.

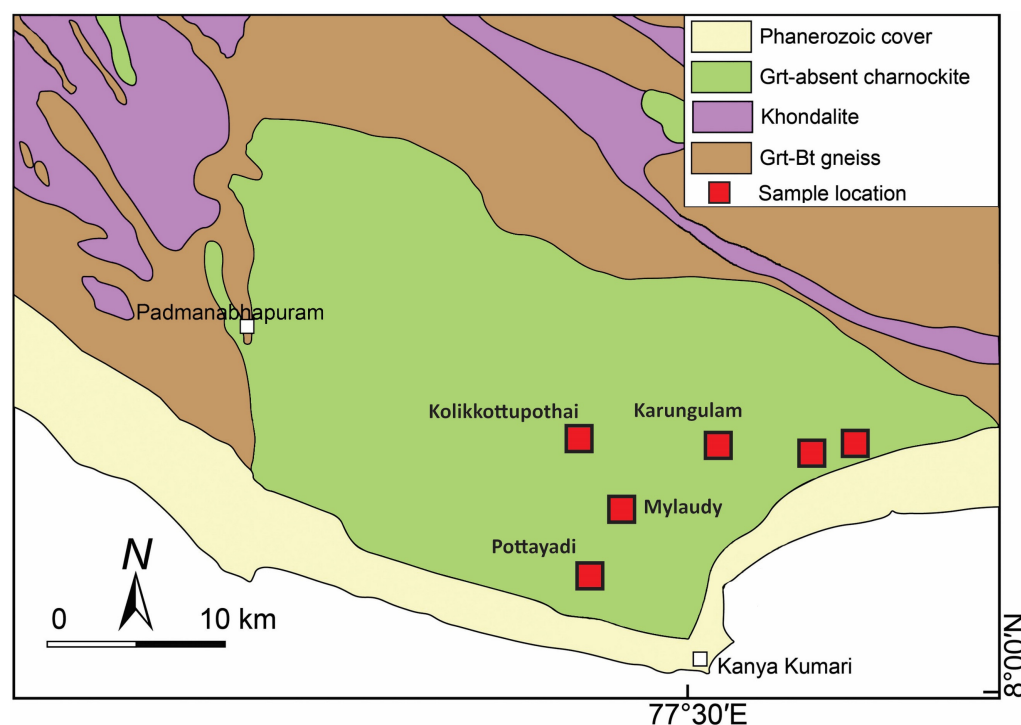


**Figure 2.** Geological map of Nagercoil block with sampling locations.

## 2. Geology of the Study Area

SGT is a collage of polydeformed crustal blocks (from north to south named Salem, Madurai, Trivandrum, and Nagercoil blocks) that are separated by crustal-scale shear zones (Figure 1) [1,2,4,6,8–10]. SGT is limited to the north by the Archaean granite-greenstone terranes of the Dharwar craton [11,12], separated by the E–W trending crustal-scale shear zone known as the Moyar Bhavani Cauvery Shear System (MBCS) [4,13]. The Salem block comprises late Archaean to early Proterozoic metamorphic and Mesoarchean to Neoproterozoic magmatic rocks [7–9,14–16]. The Madurai block, south of Salem, hosts charnockite massifs, granitoids, migmatites, metapelites, quartzites, calc silicates, and alkaline intrusives with emplacement and metamorphic ages ranging from Archean to Neoproterozoic [4,17]. Two major shear zones dissect the Madurai block, namely the Karur-Kambam-Teni-Painavu-Trissur shear zone (KKPTSZ) [9] and Suruli shear zone (SSZ) [18]. This crustal block is also known for the preservation of Ediacaran–Cambrian UHT metamorphic rocks with P–T estimates up to 1100 °C and 12 kbar with clockwise/anticlockwise P–T evolution [3,19–23]. The Madurai block is separated from the southern Trivandrum and Nagercoil blocks by the Achankovil shear zone (ASZ) [24,25], which is marked by a distinct younger whole-rock Nd model age (1.5–1.2 Ga) [17,26–28] and U–Pb zircon age (1.5–0.95 Ga) [2,29,30].

In the earlier literature, the Trivandrum–Nagercoil blocks and Achankovil shear zone were considered a large supracrustal belt named the Kerala Khondalite Belt (KKB) [31,32]. The Trivandrum block is dominated by granitoid leucogneisses and garnetiferous metasediments, whereas massive charnockites and metamorphosed mafic rocks dominate the Nagercoil block. Both these blocks share similar Rb–Sr, Sm–Nd whole-rock, as well as U–Pb zircon ages [2,9,17,26,28,33–37], all indicating their contiguity. U–Pb zircon data for the charnockite protoliths from these domains report Paleoproterozoic (ca., 1.85 Ga) emplacement ages with Orosirian juvenile magmatic signatures [2,36,37]. The well-preserved, protracted Ediacaran–Cambrian metamorphism is exposed by in situ chemical and isotopic analysis of monazite and zircon from different lithologies across these domains [35,38].

### 3. Field Relation and Petrography

For the present study, seven gabbro samples from different parts of the Nagercoil block were collected (Figure 2). These rocks form meter-scale-thick intrusions/enclaves within charnockites with widths up to two meters, occasionally forming pinch and swell structures (Figure 3a). Chilled margin contacts exist between the charnockite and mafic rocks (Figure 3b). Occasionally, coarse-grained pegmatoidal charnockites are also noticed parallel to these mafic bands. Field occurrence suggests that the rocks were subjected to a later-stage deformation after their emplacement into the host charnockite. Under the microscope, the samples exhibit interlocking grains with orthopyroxene, clinopyroxene, hornblende, plagioclase, and opaques (mostly ilmenite) (Figure 4a,b) and a minor amount of quartz. Biotite (up to 2%) is found only in two samples and is found as long, slender, and pale-yellow grains, occasionally cross-cutting orthopyroxene and clinopyroxene. At places, clinopyroxenes show an exsolution pattern typical of low Ca varieties (Figure 4c). Crystals and blebs of K-feldspar within plagioclase are also observed in the matrix (Figure 4d). Accessory phases mainly constitute zircon and apatite.

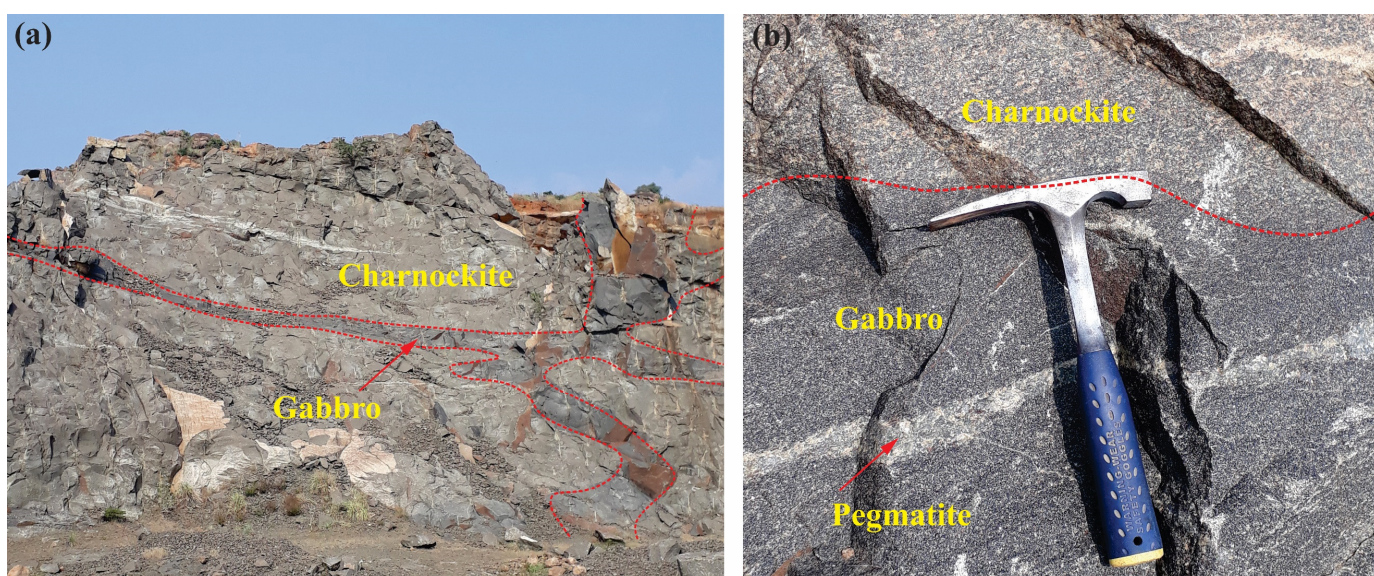


**Figure 3.** Field photographs of gabbros from Nagercoil block. (a) Gabbro band within massive charnockite; (b) Contact between gabbro and charnockite.

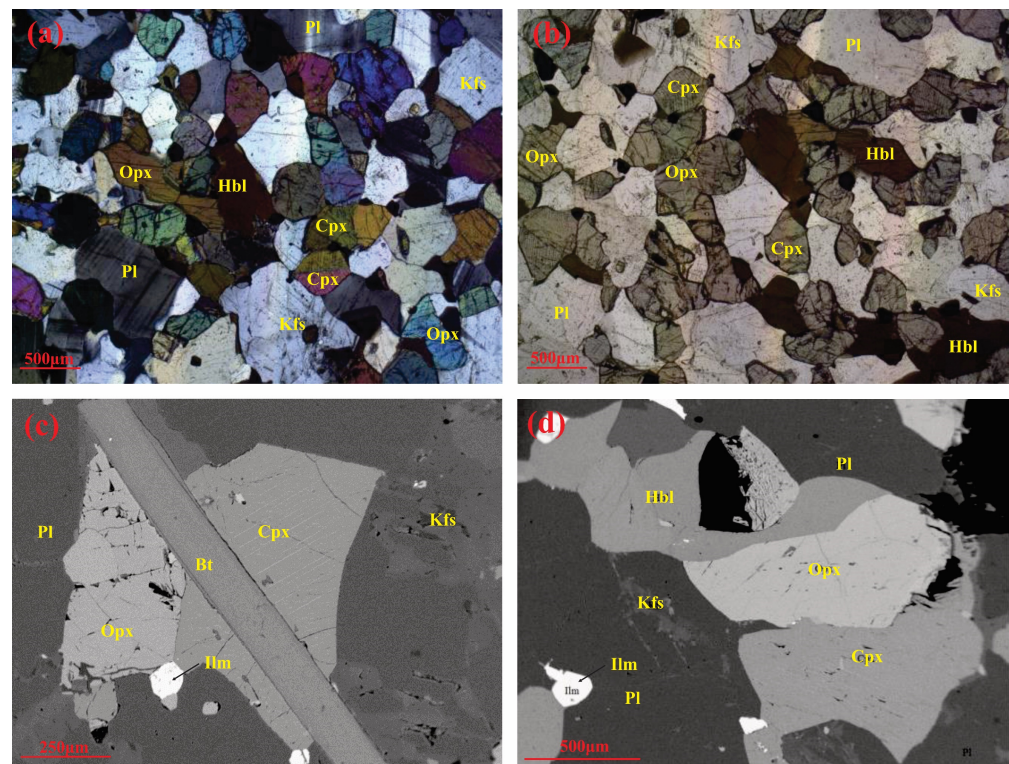


**Figure 4.** (a,b) Photomicrographs illustrating major mineral assemblages in gabbros; (c) Biotite cross-cutting orthopyroxene and clinopyroxene; (d) Crystals and blebs of K-feldspar within plagioclase associated with orthopyroxene and clinopyroxene.

#### 4. Major and Trace Element Geochemistry

The major element concentration of six samples was analysed using a Bruker Pioneer S8 Tiger WD-XRF at NCESS following the analytical protocol described in [22]. For trace element determination, these sample powders were dissolved in a reagent grade HF:HNO<sub>3</sub> acid mixture in Savillex screw-top vessels. These solutions were analysed using an Agilent 7800 Quadruple ICP-MS at the LAM-ICPMS facility at the National Geophysical Research Institute, Hyderabad. <sup>103</sup>Rh was used as the internal standard for sample analysis. During the analytical session, standards G-2, JG-2, GA, and AGV-2 were repeatedly analysed to ensure drift correction and calibration. Major and trace element plots were prepared using GCDkit 5.0 [39] by utilising the chondrite values from [40] and primitive mantle values from [41]. Geochemical data of the samples are presented in Supplementary material 1.

The samples are characterised by low SiO<sub>2</sub> (48.16–51.73 wt %), TiO<sub>2</sub> (0.82–1.61 wt %), Al<sub>2</sub>O<sub>3</sub> (13.61–16.47 wt %), MnO (0.15–0.22 wt %), CaO (9.03–9.79 wt %), moderate and varying FeO<sub>T</sub> (10.11–16.23 wt %), MgO (4.9–7.66 wt %), and Na<sub>2</sub>O (2.69–3.47 wt %) and low amounts of K<sub>2</sub>O (0.64–1.13 wt %) and P<sub>2</sub>O<sub>5</sub> (0.17–0.36 wt %). The Mg number is low and varies from 39 to 60. Moreover, these samples display low Ni (44.91–114.3 ppm) and Cr (114.6–250.2 ppm), moderate V (175.7–364 ppm), and a limited amount of Sc (40.35–53.59 ppm). In the TAS diagram (the silica versus total alkali) (Figure 5a) [42], the samples fall within the gabbro field, whereas the tholeiitic nature of the studied samples is demonstrated in the AFM diagram (Figure 5b) [43]. Chondrite-normalised REE patterns of the samples are characterised by LREE enrichment (Sm<sub>N</sub>/La<sub>N</sub> = 0.80–0.36) and near-flat to slightly fractionated HREE (Lu<sub>N</sub>/Gd<sub>N</sub> = 0.84–0.40) with slightly negative Eu (Eu/Eu\* = 1.03–0.74) and weakly positive Ce anomalies (Ce/Ce\* = 1.05–0.98) (Figure 6a). The primitive mantle-normalised multi-element variation diagram shows relative enrichment of large ion lithophile elements (LILEs) and weakly negative anomalies of high-field-strength elements (HFSEs), including Nb, Zr, and Ti (Figure 6b).

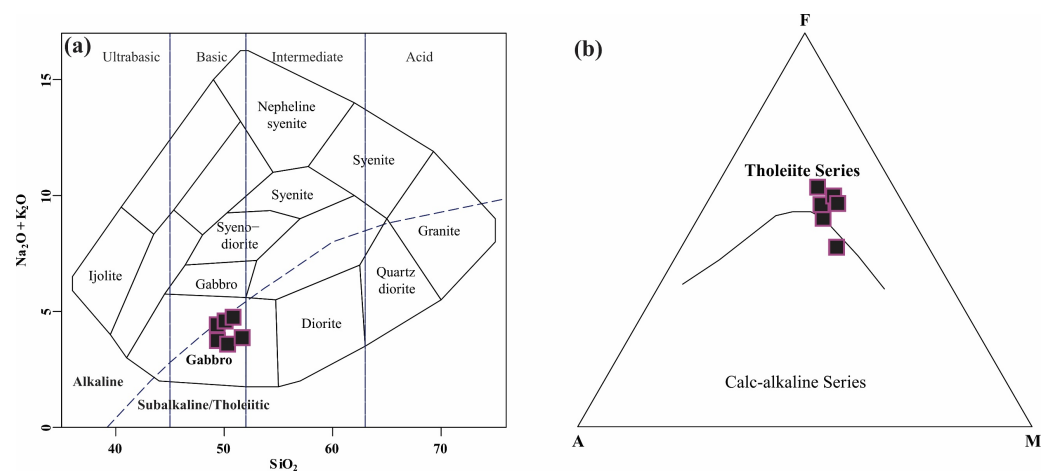


Figure 5. (a) TAS diagram [42]; (b) AFM diagram [43].

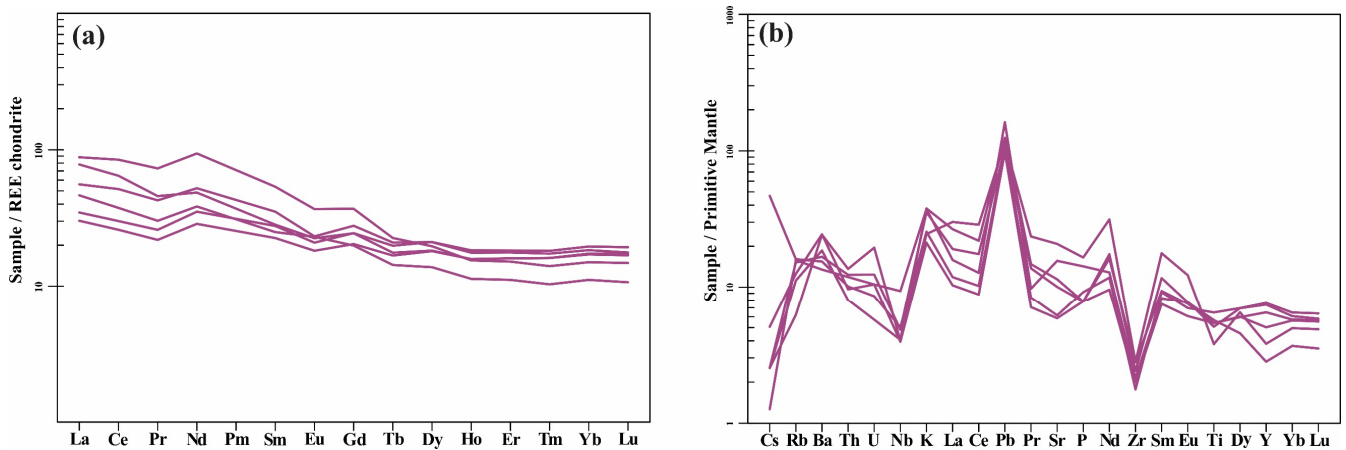
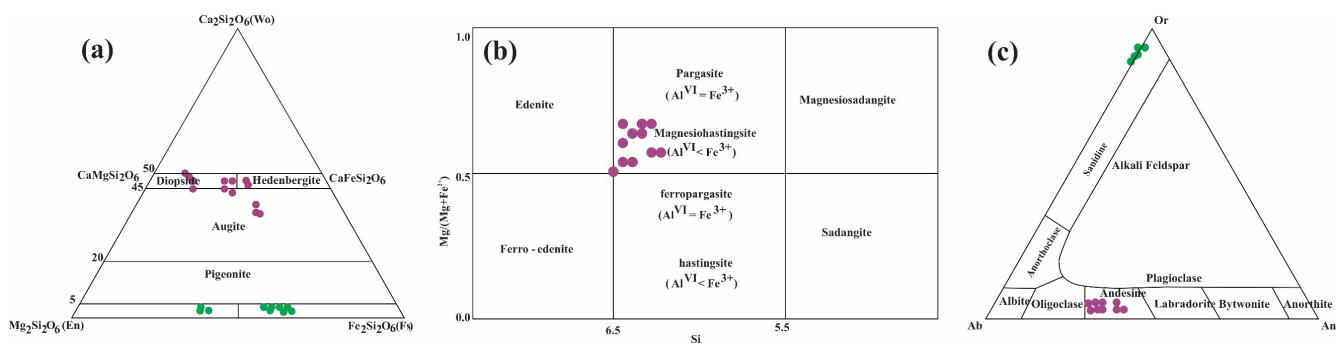


Figure 6. (a) Chondrite-normalised REE diagram of gabbros; (b) primitive-mantle-normalised trace element diagrams of gabbros.

## 5. Mineral Chemistry

Three representative samples were analysed for mineral chemistry using CAMECA SX-100 EPMA at the Department of Geology and Geophysics, Indian Institute of Technology, Kharagpur. The instrument was operated at an accelerating voltage of 15 kV, 20 nA beam current, and 1–2  $\mu\text{m}$  beam diameter. Natural silicate and oxide standards were used for calibration, and raw data were corrected using the ZAF program. EPMA data of different mineral phases are provided in Supplementary material 2.

**Pyroxenes:** Pyroxene from the samples show a near-homogeneous chemical composition across different samples. Orthopyroxenes are characterised by low  $\text{Al}_2\text{O}_3$  (1.45–0.47 wt%) with  $X_{\text{Mg}}$  ranging between 0.59 and 0.47. Similar to orthopyroxenes, clinopyroxenes from the studied samples have low  $\text{Al}_2\text{O}_3$  contents (2.71–1.82 wt%) with  $X_{\text{Mg}}$  ranging between 0.69 and 0.58. In the pyroxene classification diagram, most of the clinopyroxenes fall within the diopside-augite field, whereas orthopyroxenes show intermediate composition between enstatite and ferrosilite (Figure 7a).



**Figure 7.** (a) Wollastonite-enstatite-ferrosilite diagram showing compositions of orthopyroxene (green circle) and clinopyroxene (maroon circle). (b) Anorthite-albite-orthoclase diagram showing compositions of orthoclase (green circle) and plagioclase (maroon circle), (c) Si (pfu) vs.  $X_{Mg}$  diagram showing compositions of calcic amphibole.

**Amphiboles:** Amphiboles from the samples are characterised by high  $Al_2O_3$  contents varying between 10.77 and 0.987 wt%. The high Ca and (Na + K) contents (1.95–1.89 pfu and 0.90–0.78 pfu, respectively) classify them as calcic amphiboles. In the amphibole classification diagram (Figure 7b), the studied calcic amphiboles fall within the field of magnesiohastingsite with an  $X_{Mg}$  value ranging between 0.65 and 0.59.

**Feldspar:** Feldspar is dominantly plagioclase and is high in Na with an average composition of  $An_{40-49} Ab_{49-58} Or_{2-4}$ . K-feldspar is also identified in two samples with an average composition of  $Or_{96-97} Ab_{3-4} An_0$  (Figure 7c).

**Biotite:** Biotite is restricted to two samples with near-homogeneous composition and is characterised by high  $TiO_2$  contents (up to 4.84 wt%) with  $X_{Mg}$  values ranging between 0.64 and 0.68.

## 6. Zircon U-Pb Ages, Trace Element, and Hf Isotopes

Zircons from the samples were separated using the conventional Wilfley table-magnetic separation technique. Separated grains were manually handpicked, mounted on a standard epoxy disc of 25 mm diameter, and polished to expose their internal structure. The grains were further examined by cathodoluminescence (CL) and Backscatter Electron (BSE) imaging using a TESCAN Vega4 scanning electron microscope at NGRI, Hyderabad. U-Pb isotope and trace element analyses of zircons were performed at the Isotope Geochemistry Facility (IGF), NCESS, using a Teledyne CETAC, Nd: YAG (213 nm) solid-state laser coupled with an Agilent 7800 quadrupole ICPMS. The analytical protocol was according to [21]. For U-Pb analysis, the 91500 zircon [44] was used as the primary standard, whereas Plesovice [45] and BB11 zircon [46] were monitored for quality checks. Data reduction and the calculation of ratios and ages were performed offline using Iolite 4.4 [47] and the calculated isotopic ratios and elemental concentrations were processed using Isoplot 4.15 [48]. For in situ trace element determination, NIST 610 [49] was used as the primary reference standard for time-drift correction and quality monitoring, with  $^{29}Si$  (IS value = 14.98%) as the internal standard. Ti-in-zircon crystallisation temperatures [50] were calculated using  $\alpha_{SiO_2} = 1$  and  $\alpha_{TiO_2} = 0.6$ . The hafnium isotopic composition of zircons was analysed at the Isotope Geochemistry Facility (IGF), NCESS using a Teledyne CETAC, Nd: YAG (213 nm) solid-state laser coupled with a Nu Plasma 3 Multicollector ICPMS. Zircons analysed for U-Pb dating were reanalysed, and spots were positioned close to the previous crater due to spatial limitations. The analytical protocol was according to [22]. 91500 zircon [44] was used as the primary standard, whereas Plesovice [45] was monitored for quality check. Data reduction and ratios were calculated offline using the Hf isotope package in Iolite 4.4 [47]. The  $^{176}Lu$  decay constant of  $1.865 \times 10^{-11} \cdot yr^{-1}$  [51] was used to calculate initial Hf isotopic ratios ( $^{176}Hf/^{177}Hf$ ). The initial epsilon Hf and two-stage-depleted mantle model ages ( $T_{DM}$ ) were calculated using chondritic uniform reservoir (CHUR) ratios of  $^{176}Hf/^{177}Hf = 0.0332$  and  $^{176}Lu/^{177}Hf = 0.282772$  [52], and depleted mantle ratios of  $^{176}Hf/^{177}Hf = 0.283251$  [53]

and  $^{176}\text{Lu}/^{177}\text{Hf} = 0.0384$  [54]. All uncertainties were reported in  $2\sigma$  confidence levels. The zircon U-Pb, trace element, Ti-in-zircon temperatures, and Hf isotope data are presented in: Supplementary material 3, 4, and 5.

Zircons from the samples are spherical, oval, or irregular-shaped grains ranging from 80 to 200  $\mu\text{m}$  with an aspect ratio of 2:3. In CL images, they display structureless fine tree zoning or sector zoning and rarely chaotic textures with the local appearance of flow domains. Among these, some zircons show core-rim textures in which either the core or rim is homogeneous. Occasionally, the outer and inner domains also preserve well-developed oscillatory zoning with skinny bands (Figure 8).

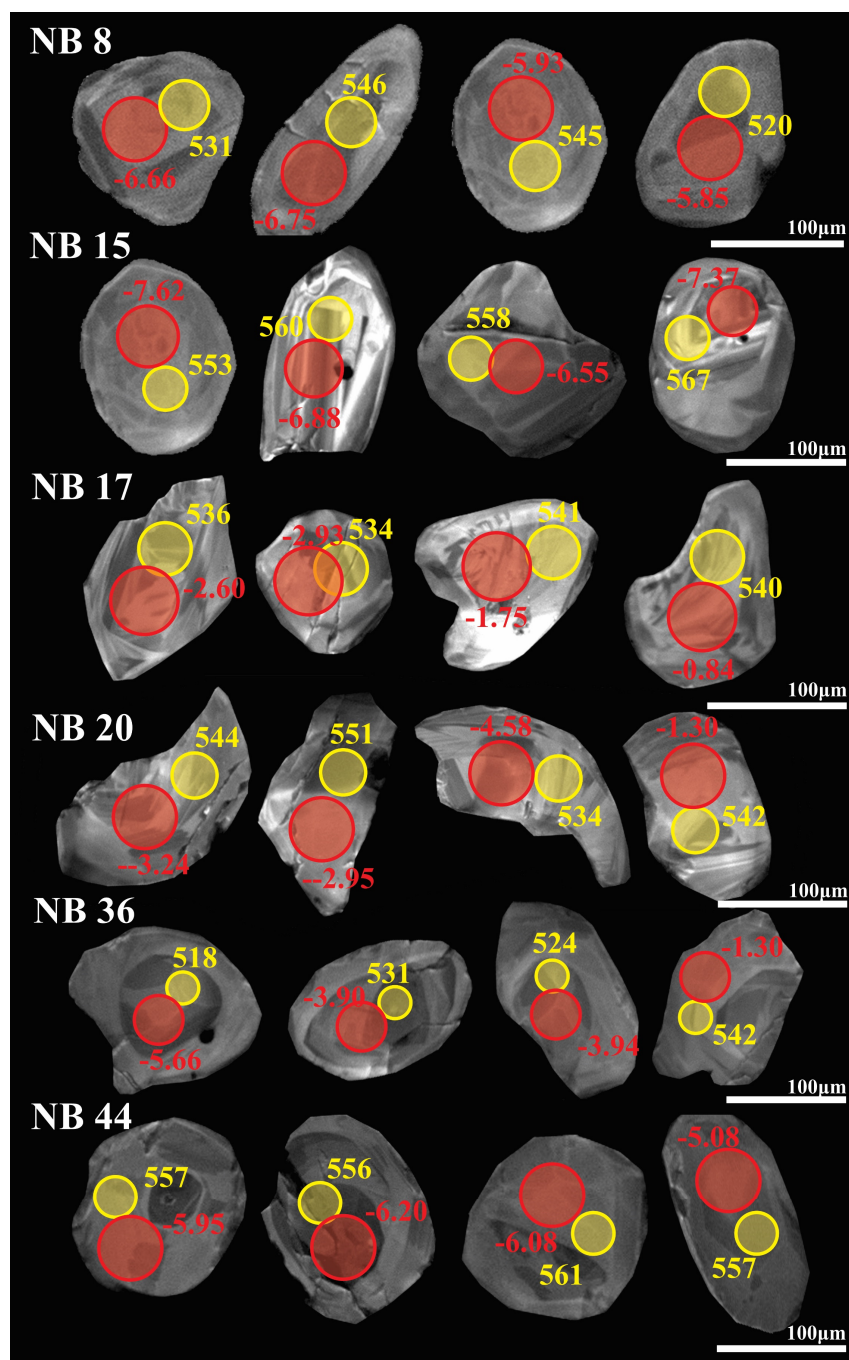


**Figure 8.** Cathodoluminescence images of selected zircon grains from gabbros. Yellow circles mark the position of the laser spot for U-Pb dating with  $^{206}\text{Pb}/^{238}\text{U}$  ages (in Ma) and red circles mark the position of Hf isotope with  $\epsilon\text{Hf}(t)$  analysis. Laser spot sizes are scaled to size.

**Sample NB8:** Twenty-one spots were analysed from the sample, which shows a Th/U distribution between 0.26 and 0.38.  $^{206}\text{Pb}/^{238}\text{U}$  ages of the sample range between 520 and 554 Ma with nineteen grains defining a weighted mean  $^{206}\text{Pb}/^{238}\text{U}$  age of  $529 \pm 4$  Ma (MSWD = 3.3). Additionally, thirteen grains represent a coherent concordia population at  $531 \pm 4$  Ma (MSWD = 1.4), which is in agreement with the weighted mean age (Figure 9a). Chondrite-normalised REE patterns of zircons display strongly positive Ce ( $\text{Ce}/\text{Ce}^* = 79.5\text{--}5.2$ ) and weakly negative Eu ( $\text{Eu}/\text{Eu}^* = 1.1\text{--}0.09$ ) anomalies together with LREE depletion and HREE enrichment (Figure 10a). The Ti concentration in zircons ranges between 23.9 and 2.8 ppm, estimating Ti-in-zircon temperatures between 894 and 678 °C. The Hf isotopic composition of zircons shows initial  $^{176}\text{Hf}/^{177}\text{Hf}$  values between 0.282311 and 0.282191 with  $\epsilon\text{Hf}(t)$  ranging between  $-4.64$  and  $-9.26$  (Figure 11a), whereas  $T_{\text{DM}}$  ages of the samples are between 1.47 and 1.30 Ga (Figure 11b).

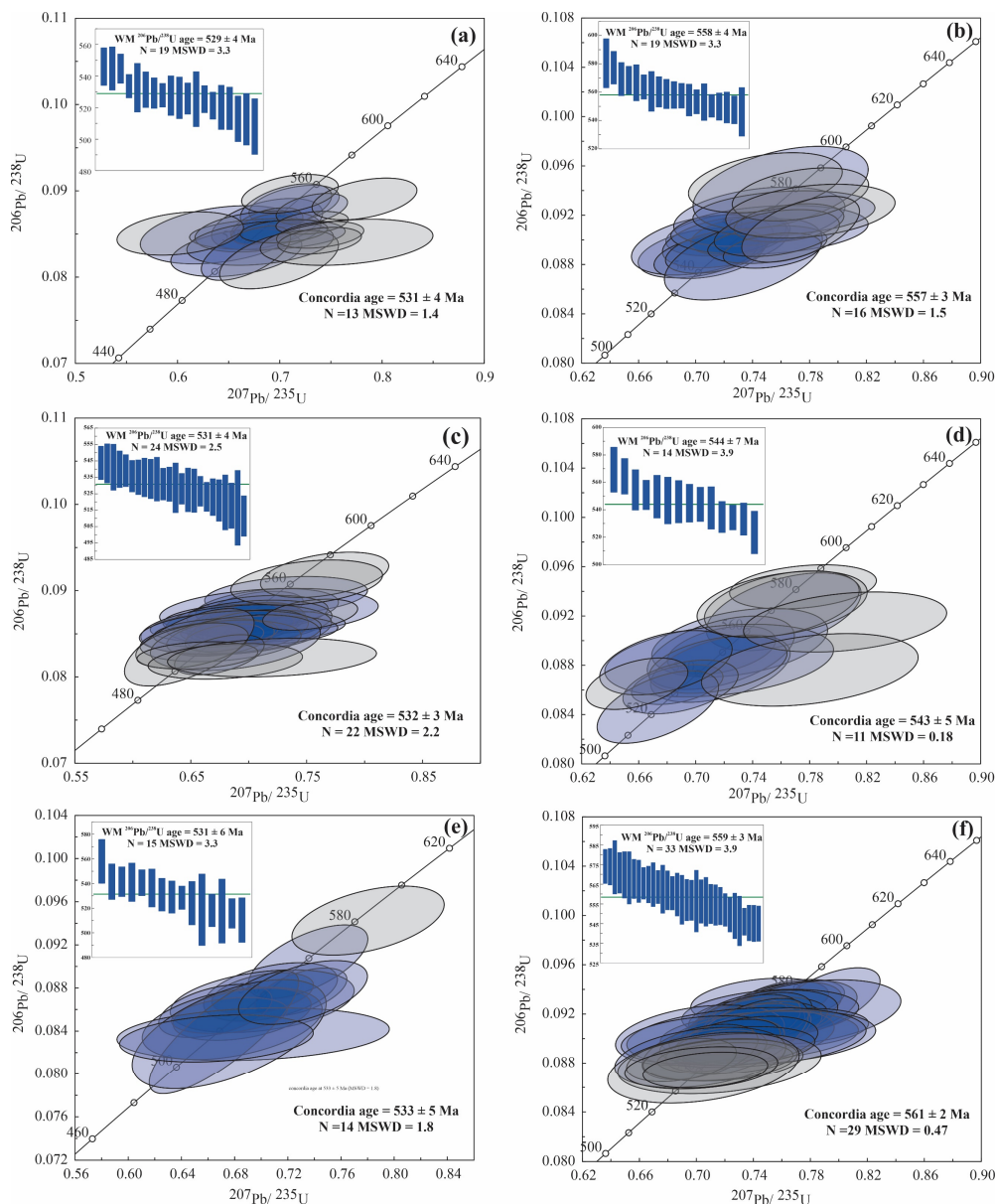


**Figure 9.** (a–f): U–Pb geochronological data of zircons analysed from gabbros presented in Wetherill diagrams: (a) NB8, (b) NB15, (c) NB17, (d) NB20, (e) NB36, and (f) NB44. Blue circles represent concordia population and grey circles represent discordant spots. Inset shows weighted mean  $^{206}\text{Pb}/^{238}\text{U}$  ages.

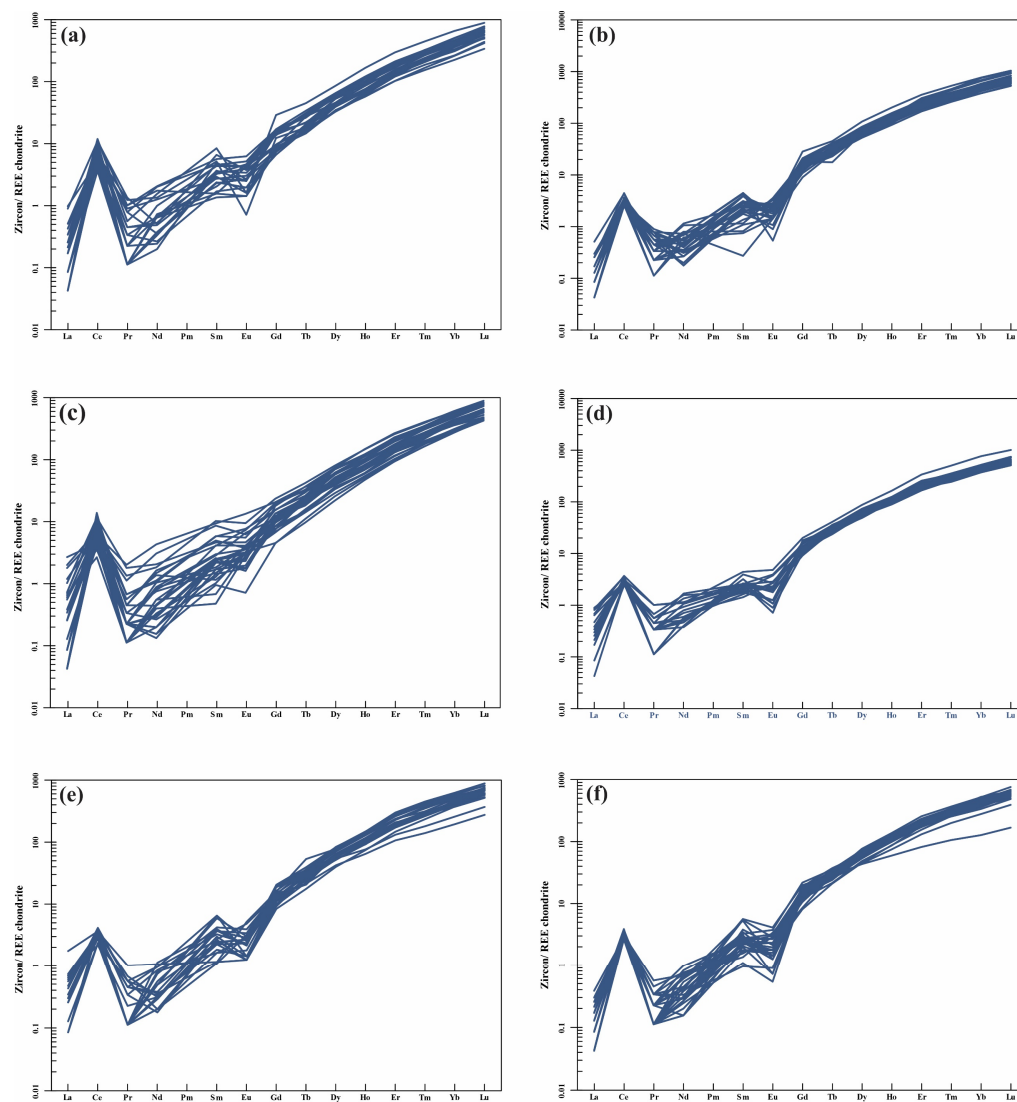


**Figure 10.** (a–f): Chondrite-normalised REE pattern of zircons from gabbros: (a) NB8, (b) NB15, (c) NB17, (d) NB20, (e) NB36, and (f) NB44.

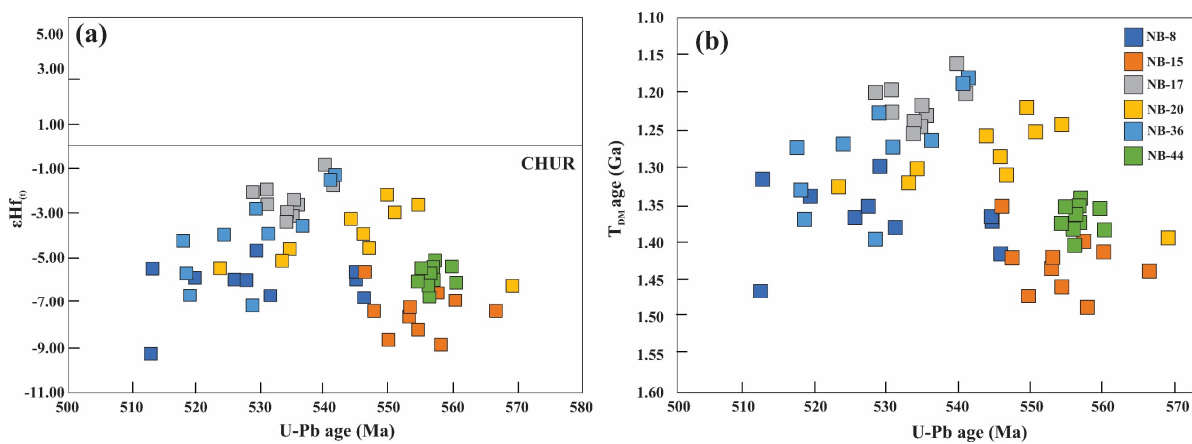


**Figure 11.** (a) Age vs.  $\epsilon\text{Hf}(t)$  of zircons; (b) U-Pb age diagram vs.  $T_{\text{DM}}$  age. Legend given in Figure 11b.

**Sample NB15:** Twenty spots analysed from the samples display  $^{206}\text{Pb}/^{238}\text{U}$  ages between 546 and 583 Ma with Th/U ratios ranging between 0.24 and 0.31. Nineteen spots among these define a weighted mean  $^{206}\text{Pb}/^{238}\text{U}$  age of  $558 \pm 4$  Ma (MSWD = 3.3), which is supplemented by a concordia age of  $557 \pm 3$  Ma (MSWD = 1.5) defined by sixteen spots (Figure 9b). Chondrite-normalised REE patterns of zircons from the sample display LREE depletion and HREE enrichment with strongly positive Ce ( $\text{Ce}/\text{Ce}^* = 22.8\text{--}5.5$ ) and weakly negative Eu ( $\text{Eu}/\text{Eu}^* = 0.78\text{--}0.16$ ) anomalies (Figure 10b). The Ti concentration in zircons ranges between 13.5 and 4.0 ppm, estimating Ti-in-zircon temperatures between 828 and 709 °C. The Hf isotopic composition of zircons shows initial  $^{176}\text{Hf}/^{177}\text{Hf}$  values between 0.282274 and 0.282174 with  $\epsilon\text{Hf}_{(t)}$  ranging between  $-5.60$  and  $-8.86$  (Figure 11a), whereas  $T_{\text{DM}}$  ages of the samples are between 1.49 and 1.35 Ga (Figure 11b).

**Sample NB17:** Thirty spots analysed from the samples show Th/U ratios between 0.21 and 1.04 and  $^{206}\text{Pb}/^{238}\text{U}$  ages between 507 and 566 Ma. Among these, twenty-four spots from the sample define a weighted mean  $^{206}\text{Pb}/^{238}\text{U}$  age of  $531 \pm 4$  Ma (MSWD = 2.5), whereas twenty-two grains define a concordia population at  $532 \pm 3$  Ma (MSWD = 2.2) (Figure 9c). Chondrite-normalised REE patterns of zircons display LREE depletion and HREE enrichment with strongly positive Ce ( $\text{Ce}/\text{Ce}^* = 106\text{--}3.2$ ) and weakly negative Eu ( $\text{Eu}/\text{Eu}^* = 1.5\text{--}0.29$ ) anomalies (Figure 10c). The Ti concentration in zircons ranges between 19.8 and 2.8 ppm, estimating Ti-in-zircon temperatures between 872 and 679 °C. The Hf isotopic composition of zircons shows initial  $^{176}\text{Hf}/^{177}\text{Hf}$  values between 0.282412 and 0.282344 with  $\epsilon\text{Hf}_{(t)}$  ranging between  $-0.84$  and  $-3.37$  (Figure 11a), whereas  $T_{\text{DM}}$  ages of the samples are between 1.26 and 1.16 Ga (Figure 11b).

**Sample NB20:** Seventeen spots analysed from the samples demonstrate the  $^{206}\text{Pb}/^{238}\text{U}$  age spread between 5024 and 581 Ma with Th/U ratios between 0.27 and 0.41. Fourteen spots among these define a weighted mean  $^{206}\text{Pb}/^{238}\text{U}$  age of  $544 \pm 7$  Ma (MSWD = 3.9), which is supported by a concordia age population at  $543 \pm 5$  Ma (MSWD = 0.18) defined by eleven spots (Figure 9d). Chondrite-normalised REE patterns of zircons show LREE depletion and HREE enrichment with strongly positive Ce ( $\text{Ce}/\text{Ce}^* = 34.9\text{--}3.5$ ) and weakly negative Eu ( $\text{Eu}/\text{Eu}^* = 0.73\text{--}0.11$ ) anomalies (Figure 10d). The Ti concentration in zircons ranges between 46.2 and 4.0 ppm, estimating Ti-in-zircon temperatures between 982 and 710 °C. The Hf isotopic composition of zircons shows initial  $^{176}\text{Hf}/^{177}\text{Hf}$  values between 0.282369 and 0.282242 with  $\epsilon\text{Hf}_{(t)}$  ranging between  $-2.16$  and  $-6.20$  (Figure 11a), whereas  $T_{\text{DM}}$  ages of the samples are between 1.39 and 1.22 Ga (Figure 11b).

**Sample NB36:** Sixteen spots analysed from the samples show Th/U ratios between 0.21 and 1.04 and the  $^{206}\text{Pb}/^{238}\text{U}$  age spread between 511 and 581 Ma. Fifteen spots from these define a weighted mean  $^{206}\text{Pb}/^{238}\text{U}$  age of  $531 \pm 6$  Ma (MSWD = 3.3), while fourteen grains define a concordia age at  $533 \pm 5$  Ma (MSWD = 1.8) (Figure 9e). Chondrite-normalised REE patterns of zircons display LREE depletion and HREE enrichment with strongly positive Ce ( $\text{Ce}/\text{Ce}^* = 19.5\text{--}3.5$ ) and weakly negative Eu ( $\text{Eu}/\text{Eu}^* = 1.2\text{--}0.18$ ) anomalies (Figure 10e). Ti-in-zircon temperature estimates range between 891 and 710 °C, which corresponds to a Ti concentration of 23.4 to 4.0 ppm. The Hf isotopic composition of zircons shows initial  $^{176}\text{Hf}/^{177}\text{Hf}$  values between 0.282398 and 0.282242 with  $\epsilon\text{Hf}_{(t)}$  ranging between  $-1.30$  and  $-7.12$  (Figure 11a), whereas  $T_{\text{DM}}$  ages of the samples are between 1.40 and 1.18 Ga (Figure 11b).

**Sample NB44:** Thirty-seven spots analysed from the samples exhibit Th/U ratios between 0.25 and 0.46 and  $^{206}\text{Pb}/^{238}\text{U}$  ages between 540 and 574 Ma. Thirty-three spots from this group define a weighted mean  $^{206}\text{Pb}/^{238}\text{U}$  age of  $559 \pm 3$  Ma (MSWD = 3.9), which is supplemented with a concordia age population at  $561 \pm 2$  Ma (MSWD = 0.47), defined by twenty-nine spots (Figure 9f). Zircon-chondrite-normalised REE patterns display LREE depletion and HREE enrichment with strongly positive Ce ( $\text{Ce}/\text{Ce}^* = 44\text{--}8.9$ ) and weakly negative Eu ( $\text{Eu}/\text{Eu}^* = 0.84\text{--}0.10$ ) anomalies (Figure 10f). Ti-in-zircon temperatures are estimated between 909 and 721 °C as defined by Ti concentrations between 27 and 4.6 ppm. The Hf isotopic composition of zircons shows initial  $^{176}\text{Hf}/^{177}\text{Hf}$  values between 0.282282

and 0.282235 with  $\epsilon\text{Hf}(t)$  ranging between  $-5.08$  and  $-6.74$  (Figure 11a), whereas  $T_{\text{DM}}$  ages of the samples are between 1.40 and 1.34 Ga (Figure 11b).

## 7. Discussion

### 7.1. Petrogenesis of Mafic Rocks in Nagercoil Block

The studied gabbros are characterised by their tholeiitic affinity with strong enrichment of LILE/LREE and depletion in HREE elements. These geochemical characteristics, together with negative anomalies for Zr, Hf, and Ti and high LILE-to-HFSE ratio, are suggestive of their origin in an arc-related environment, possibly by the involvement of subduction of a modified enriched mantle source [55,56]. The arc affinity of the samples is further validated by the La/Yb vs. Nb/La (Figure 12a) [57] and  $\text{TiO}_2$  vs.  $\text{Al}_2\text{O}_3$  diagram [58], where the gabbros fall within the arc field (Figure 12b). The  $\text{FeO}^*/\text{MgO}$  vs.  $\text{TiO}_2$  values of the samples indicate that they were primarily derived from the arc front [59] (Figure 12c). Furthermore, the low Nb/La (0.14–0.61) ratios of these gabbros are partly similar to those from the lithospheric mantle (0.3–0.4) rather than asthenospheric mantle ( $>1$ ), suggesting that they were likely originated from a depleted lithospheric mantle [60]. This is further demonstrated by their positive Nb and Ta anomalies [59] together with high La/Nb (7.24–1.63) and La/Ta (44.36–14.24) and low Zr/Ba (0.24–0.14) ratios [61,62]. However, a significant variation in trace element pair ratios such as Nb/U (30.87–7.05), Ta/U (3.54–1.20), and Ce/Pb (6.27–1.97) from MORB is also noticed for the samples. This is further demonstrated in the Nb/Yb vs. Th/Yb diagram [63] where the gabbros fall away from the MORB-IOB array (Figure 12d), which suggests that the composition of gabbros does not directly reflect the composition of the primary melt, rather a modified melt composition [64]. The overall trend of the sample pointing toward the volcanic arc array in the Nb/Yb vs. Th/Yb diagram suggests the influence of subduction-related processes in their generation.

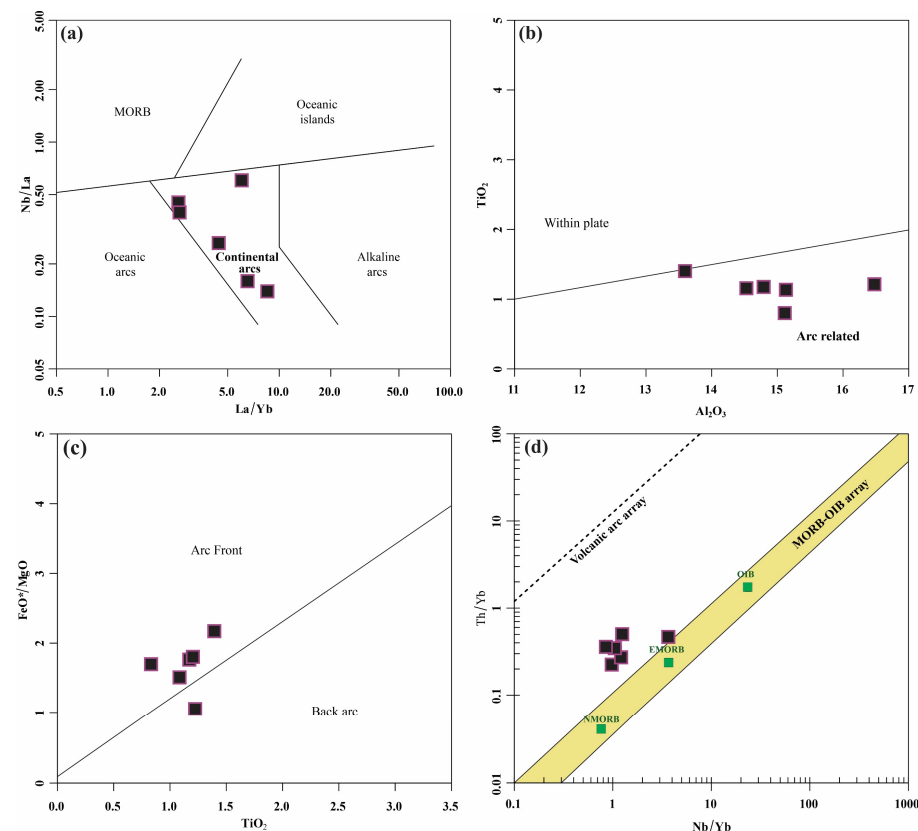


**Figure 12.** (a) La/Yb-Nb/La diagram [57]; (b)  $\text{TiO}_2$  vs.  $\text{Al}_2\text{O}_3$  diagram [58]; (c)  $\text{FeO}^*/\text{MgO}$  vs.  $\text{TiO}_2$  [59]; (d) Th/Yb vs. Nb/Yb diagram [63].

Even though the subduction-modified primary melt composition is proposed for the generation of these rocks, the extremely low Nb/Ta (<9) implies the presence of a possible contaminant in modifying their parental composition. This is further demonstrated by the wide variation in  $K_2O/P_2O_5$  (6.71–2.06) and  $TiO_2/P_2O_5$  ratios (7.00–2.28) in the sample, suggesting the incorporation of the silicic crustal component with granitic composition [65]. A close correlation with the ratios of incompatible elements such as Zr/Sm (7.52–3.98), Sm/La (0.50–0.23),  $TiO_2/Zr$  (0.07–0.03), and Th/Yb (0.48–0.25) in gabbros with the average composition of host charnockite [17] validates the involvement of basement charnockites in modifying the parental melt composition of these gabbros. To assess the extent of crustal contamination and source composition, we used assimilation and fractional crystallisation (AFC) modelling using the La/Sm vs. Lu/Yb bivariate plot (Figure 13). AFC modelling was carried out using the ‘PetroGram’ excel spreadsheet [66] where non-modal fractional melting was performed using spinel- and garnet lherzolite compositions as end members (compositions are from [67,68]). Primitive mantle (PM) values from [41] were used as the primary melt composition for constructing the AFC line, and the average composition of charnockites from the Nagercoil block [17] was used as the contaminant. The modelled output reveals that the gabbros in the Nagercoil block can be generated by ~1% to 1.5% partial melting of a mantle source composed of a ~50/50 contribution from spinel and garnet lherzolite with an AFC up to ~87%. This argument of the spinel-garnet lherzolite contribution in primary melt generation is further supported by their Ce/Y values (<2.5) that are in agreement with the primary melt generation from the spinel-garnet stability field [69].

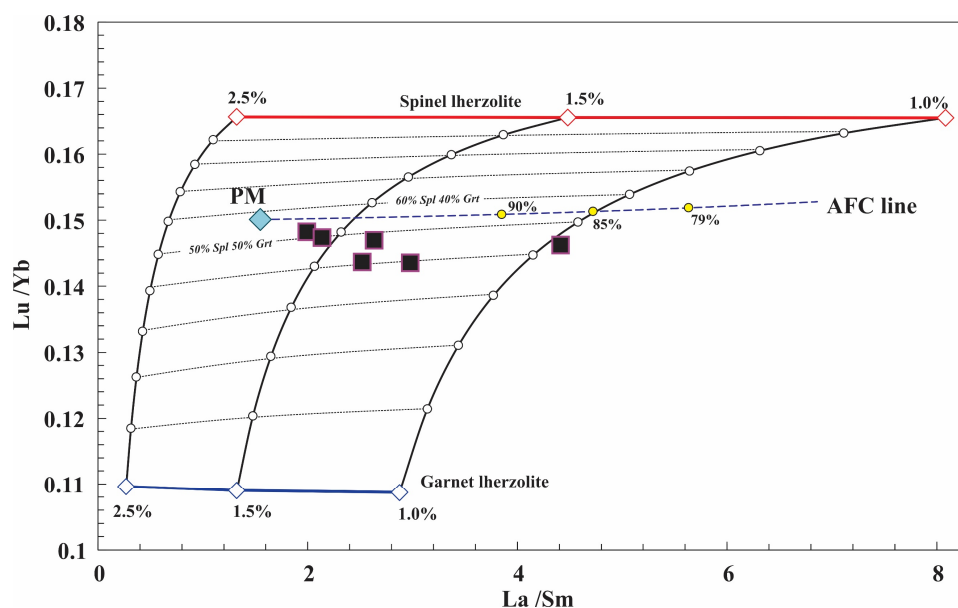


**Figure 13.** Assimilation and fractional crystallisation (AFC) model showing La/Sm vs. Lu/Yb bivariate diagram for gabbros. PM: Primitive Mantle.

## 7.2. Neoproterozoic Mafic Magmatism in Nagercoil Block and Its Tectonic Significance

Zircon grains from the gabbros are characterised by structureless fir tree to sector zoning with poorly developed core-rim structures, which is commonly found in zircons from mafic rocks [70]. The magmatic origin of these rocks is further demonstrated by their low Th/U ratios, which is also typical of zircons crystallising from mafic magmas [71]. U-Pb dating of zircons from the samples yield well-defined concordia and a coherent weighted mean population bracketed between 561 and 531 Ma. These ages can be interpreted as the timing of mafic emplacements in the terrane. These ages also closely follow the timing of granulite facies metamorphism recorded in the terrane [34–38]. The intrusive relationship of these gabbros with the host charnockites and the similarity in the timing of

their emplacement and metamorphism in the terrane suggest synchronous emplacement of these rocks with the regional-scale metamorphic event.

Trace element signatures of zircons from gabbros are characterised by LREE depletion and HREE enrichment along with prominent negative europium and positive cerium anomalies, all indicative of their igneous origin [72]. The formation of zircons in mafic rocks is rare owing to their low Zr and free SiO<sub>2</sub> concentrations. In such a scenario, zircon formation is mainly assisted by metasomatism with Zr supplied from subduction zone fluids and is expected to retain zircons from the slab residue as inherited grains [73]. In the present study, high-Hf and low-Zr/Hf-ratio zircons represent their growth in a fractionated melt [74], whereas prominent positive Ce and negative Eu anomalies indicate coeval plagioclase crystallisation. The involvement of fractional crystallisation in the zircon formation is further demonstrated by the negative correlations between Ti and Hf concentrations. Trace element signatures zircons can also be used to identify the tectonic setting for their formation. Zircons from the gabbros are characterised by their high U/Yb (>1) ratio, which indicates their arc affinity [75], whereas, in the Y vs. U/Yb zircon discrimination diagram ([76], Figure 14), all samples fall within the continental zircons field. These inferences of zircon formation during fractional crystallisation in a continental arc environment are consistent with the observations based on whole-rock geochemistry. Hafnium isotopic signatures of zircons show initial <sup>176</sup>Hf/<sup>177</sup>Hf ratios ranging between 0.282412 and 0.282174 with εHf<sub>(t)</sub> ranging between −0.84 and −9.26, whereas T<sub>DM</sub> ages fall between 1.49 and 1.16 Ga. The tight population of initial <sup>176</sup>Hf/<sup>177</sup>Hf ratios and a narrow T<sub>DM</sub> age range suggest the formation of these gabbros from a near-uniform mid-Mesoproterozoic (Ectasian) isotopic reservoir. These T<sub>DM</sub> ages are consistent with the previous studies on gabbros from the area [34]. However, they are younger than the Paleoproterozoic Hf-T<sub>DM</sub> [2,77] and Nd-T<sub>DM</sub> ages [17,31] reported from charnockites and orthogneisses in the region. The negative to near-positive εHf<sub>(t)</sub> of the zircons suggests low-degree reworking of the mid-Mesoproterozoic source for the generation of parental melt.

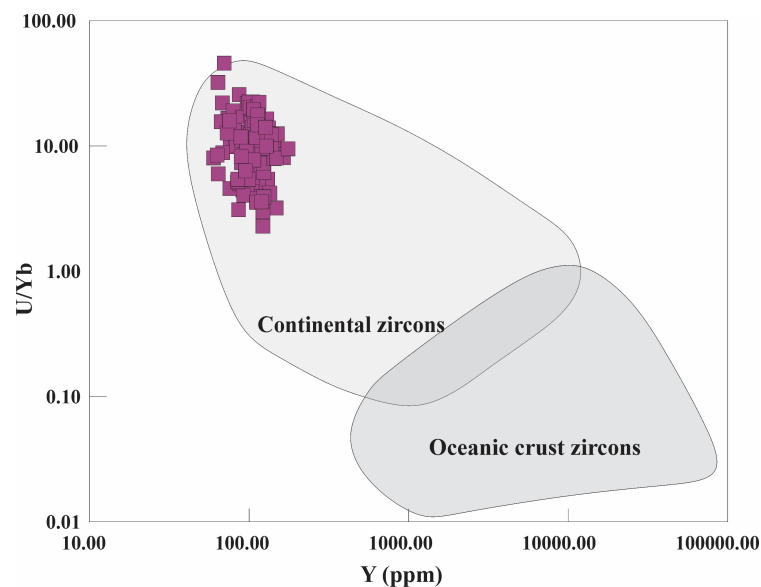


**Figure 14.** Y vs. U/Yb zircon discrimination diagram [76].

### 7.3. Geodynamic Significance

The Nagercoil block preserves three major crustal growth/metamorphic episodes: (1) 1.9 to 2.0 Ga I-type charnockite emplacement with juvenile magmatic signatures [2,34,36,37]; (2) 0.55 Ga granulite facies metamorphism [35,36,38]; (3) 0.55 mafic emplacement [34]. Traditionally, the Nagercoil block has been treated as an exotic tectonic unit with African ancestry. It resided with the Congo-Tanzania-Bangweulu continent that subsequently became amalgamated into India during the Ediacaran-Cambrian Gondwana supercon-

continent amalgamation [36]. This argument was strictly based on the lack of a 1.9–2.0 Ga magmatic/metamorphic record elsewhere in the south Indian shield. Alternatively, the Nagercoil block was also proposed as a Paleoproterozoic magmatic arc generated with the subduction-collision of crustal fragments within the Columbia supercontinent [37], which is further validated by the increased recognition of 1.9 Ga magmatic/metamorphic episodes from other parts of SGT [22,56]. As contrasting models have been proposed for the tectonic evolution of the Nagercoil block, the present study attempts to address the issue based on the new data generated for gabbros along with available results published so far from the terrane.

Based on the new geochemical and zircon U-Pb/trace element fingerprinting of the samples, it can be interpreted that the parental melts of these gabbros were generated by the partial melting of the subduction-modified lithospheric mantle source, emplaced and subsequently metamorphosed to granulite facies conditions between 561 and 531 Ma. The present tectonic models proposed for the emplacement of gabbros in the adjacent Trivandrum block argues for a collision between Madurai and Nagercoil blocks during the East African collisional orogeny resulting in subduction, slab breakoff, and asthenospheric upwelling processes along the Achankovil shear zone during the late Neoproterozoic period [6,59]. However, a similar model cannot be envisaged for the samples from Nagercoil, considering the Hf- $T_{DM}$  model ages of these gabbros. Hf- $T_{DM}$  model ages of the samples range from 1.16 to 1.48 Ga, pointing to a mid-Mesoproterozoic melting source. Available Hf- $T_{DM}$  and Nd- $T_{DM}$  model ages from Madurai and Nagercoil blocks are dominantly Paleoproterozoic [2,17,22,34,37,78], except for the eastern part of central Madurai and southeastern part of Madurai and Trivandrum blocks [2,17,30,31]. Among these, rocks from the eastern part of the central Madurai block are reported with Cryogenian emplacement ages and negative  $\epsilon Hf(t)$  signatures (moderately reworked). In contrast, the Tonian rocks from SE Madurai and Trivandrum blocks (roughly equivalent to the Achankovil unit [31]) are characterised by positive to near-positive  $\epsilon Hf(t)$  signatures (juvenile to less reworked) [2,30,79,80]. These domains also fall within the youngest Nd-model aged terrane in the SGT, with Nd- $T_{DM}$  ages ranging between 2000 and 1200 Ma [17]. Considering the source age and  $\epsilon Hf(t)$  values of studied gabbros, a mid-Mesoproterozoic melting source with a juvenile to less reworked signature is required for their formation. These requirements agree with the isotopic characteristic of the Achankovil unit [31]. Hence, Neoproterozoic subduction along the ASZ is unlikely as this could generate gabbros either with juvenile isotopic signatures or with moderately to strongly reworked isotopic signatures with Paleoproterozoic melting source age. A similar argument can also be proposed for the emplacement of gabbros in the Trivandrum block, considering their similarities in geochemistry and emplacement age. However, the idea remains ambiguous due to the lack of zircon Hf isotopic data from gabbros in the Trivandrum block.

As these gabbros are interpreted to be formed by the melting of a mid-Mesoproterozoic source, possibly contributed from the southeastern Achankovil unit, the formation of these rocks in the Nagercoil block can be explained in connection with the tectonic evolution of the Achankovil unit. The Achankovil unit represents a younger Nd-model-age terrane reported with Tonian U-Pb ages and juvenile Hf isotopic signatures [2,17,30,31]. Based on the age and isotopic signatures, the Achankovil unit has been previously correlated with the Wannu Complex of Sri Lanka [26,31], although recent studies suggest a linkage between the Wannu Complex and eastern Madurai block [4,34,78,81,82]. In this context, the correlation of the Achankovil unit with its Sri Lankan counterpart remains enigmatic. An alternative is the Vijayan complex of Sri Lanka, a Grenville age magmatic suit predominantly emplaced between 1100 and 1000 Ma with mid- to early-Mesoproterozoic Hf and Nd model ages [77]. However, the formation of the Vijayan complex is correlated with the formation of the Rodinia supercontinent [77]. Hence, a scenario can be assumed where the mid-Mesoproterozoic subduction-modified melting source responsible for the formation of gabbros in Nagercoil (and Trivandrum block) could have been contributed by the active subduction process operated along the southeastern margin of accreted India

and Sri Lanka that resulted in the formation of the Vijayan complex and Achankovil unit during Rodinia assembly. This argument is further supported by the age and isotopic characteristics of gabbros reported from the Highland Complex of Sri Lanka, which are proposed to be formed by subduction-collision tectonics operated between Highland and Vijayan complexes during the mid-Neoproterozoic [83].

#### *7.4. Gabbros from Nagercoil Block: An Alternate Heat Source for Neoproterozoic Regional-Scale High-T Metamorphism*

SGT (mainly Madurai and Trivandrum blocks) is known for the prolific preservation of Neoproterozoic high- to ultrahigh-temperature metamorphic rocks with a generalised clockwise P-T trajectory [3,22,84]. These HT-UHT metapelites are prominently distributed along the Suruli shear zone in the Madurai block (also known as the Kambam UHT belt) [4,19,21–23] and Trivandrum/Achankovil shear zones [35,85–87], which are ascribed to be formed during the collisional orogen prevalent during the final stage of the Gondwana supercontinent assembly [3,5,19,22]. The presence of Neoproterozoic HT-UHT metamorphism is not only restricted to SGT but also spread throughout other Gondwanan fragments, including Antarctica [88], Sri Lanka [89], and Madagascar [90]. In such collisional orogens, the formation of regional-scale UHT metamorphic rocks can be designated to develop different tectonic scenarios [91]. In SGT and other Gondwanan terranes, the heat source models for UHT rock formation have been poorly explored. Recent studies from the Madurai block suggest that the UHT metamorphism in the terrane resulted from crustal thickening and HPE enrichment, based on 1-D numerical modelling [3]. However, an alternate model has been proposed, suggesting coeval mafic magmatism as the possible heat source for regional-scale UHT metamorphism [23].

Other than Madurai, the Trivandrum block proximal to the Nagercoil block is also reported for HT-UHT metapelites with metamorphic conditions reaching up to P-T values of 5–9.5 kbar and 700–1040 °C [27,81,86,87,92]. Numerical modelling studies [93] suggest that granulite formation in the Trivandrum block exclusively by HPE enrichment is unlikely without adding heat from an external source. Considering these aspects, the coeval mafic emplacements reported from the Nagercoil block [34] and Trivandrum block [59] can be proposed as an alternative heat source for HT-UHT granulite formation in the area. This assumption cogitates the fact that voluminous, syn-metamorphic mafic or ultramafic emplacements reported in regional-scale granulite terranes can be considered a primary heat source for HT-UHT granulite formation [94–97]. This argument is further supported by the close spatial association as well as coeval emplacement ages of mafic granulites with regional-scale HT-UHT granulites across different Gondwana fragments including the Madurai block (our data, under review), Sri Lanka [83,98], and Antarctica [99], characterising Neoproterozoic mafic emplacement as a pervasive event recorded across east Gondwana fragments.

## **8. Conclusions**

Petrology, geochemistry, and U-Pb/Hf geochronology of gabbros from the Nagercoil block, south India provide a detailed understanding about their age, petrogenesis, and tectonic significance. The gabbros were formed by the partial melting of a subduction-modified lithospheric mantle source with a 50/50 contribution from spinel/garnet lherzolite in a continental arc setting. LA-ICPMS U-Pb zircon ages constrain their emplacement between 561 and 531 Ma. LA-MC-ICPMS zircon hafnium isotopic studies reveal near-juvenile magmatic signatures with mid-Mesoproterozoic Hf-T<sub>DM</sub> model ages. These results provide pristine evidence for the genetic linkage between gabbros and the Achankovil unit of south India, where the latter is perceived as the contributor of melting source. The age, geochemistry, and isotopic characteristics of the gabbros enable correlation with similar rock types from Sri Lanka, suggesting their coeval evolution. The study also suggests mafic magmatism as an alternative heat source for regional-scale HT-UHT metamorphism pervasive across Gondwanan terranes.

**Supplementary Materials:** The following supporting information can be downloaded at: <https://www.mdpi.com/article/10.3390/min12121509/s1>, Supplementary material 1: Whole rock geochemical data of gabbros; Supplementary material 2: Representative mineral chemistry data of gabbros; Supplementary material 3: U-Pb zircon data of gabbros; Supplementary material 4: Zircon REE data; Supplementary material 5: Zircon Hf isotope data.

**Author Contributions:** Conceptualization: S.S. and J.K.T.; methodology: S.S., J.K.T., J.A.D., N.S. and T.V.K.; formal analysis: S.S., J.K.T., J.A.D., N.S. and T.V.K.; investigation: S.S., J.K.T., J.A.D., N.S. and T.V.K.; resources: S.S., J.K.T., J.A.D., N.S. and T.V.K.; writing—review and editing: S.S., J.K.T., J.A.D. and N.S.; visualization: S.S., J.K.T., J.A.D. and N.S. All authors have read and agreed to the published version of the manuscript.

**Funding:** This research received no external funding.

**Data Availability Statement:** Not applicable.

**Acknowledgments:** The authors thank the Director, NCESS, for encouragement and support. K. Eldhose, N. Nishanth, G. Lekshmi, Sarath Kumar S, and Sribin C are acknowledged for support during fieldwork, sample preparation, and analysis. Sajna S gratefully acknowledges PhD research funding through the CSIR research fellowship program. B. Mishra and Saptarshi at IIT, Kharagpur are thanked for EPMA analysis at the National EPMA Facility, IIT Kharagpur. TVK acknowledges the financial support from an in-house project MLP-6406-28(EVB) and thanks the Director, CSIR-NGRI for his continuous support and encouragement.

**Conflicts of Interest:** The authors declare no conflict of interest.

## References

1. Talukdar, M.; Sarkar, T.; Sengupta, P.; Mukhopadhyay, D. The Southern Granulite Terrane, India: The Saga of over 2 Billion Years of Earth's History. *Earth Sci. Rev.* **2022**, *232*, 104157. [[CrossRef](#)]
2. Vijaya Kumar, T.; Bhaskar Rao, Y.J.; Plavsa, D.; Collins, A.S.; Tomson, J.K.; Vijaya Gopal, B.; Babu, E.V.S.S.K. Zircon U-Pb Ages and Hf Isotopic Systematics of Charnokite Gneisses from the Ediacaran–Cambrian High-Grade Metamorphic Terranes, Southern India: Constraints on Crust Formation, Recycling, and Gondwana Correlations. *Bull. Geol. Soc. Am.* **2017**, *129*, 625–648. [[CrossRef](#)]
3. Clark, C.; Healy, D.; Johnson, T.; Collins, A.S.; Taylor, R.J.; Santosh, M.; Timms, N.E. Hot Orogens and Supercontinent Amalgamation: A Gondwanan Example from Southern India. *Gondwana Res.* **2015**, *28*, 1310–1328. [[CrossRef](#)]
4. Brandt, S.; Raith, M.M.; Schenk, V.; Sengupta, P.; Srikantappa, C.; Gerdes, A. Crustal Evolution of the Southern Granulite Terrane, South India: New Geochronological and Geochemical Data for Felsic Orthogneisses and Granites. *Precambrian Res.* **2014**, *246*, 91–122. [[CrossRef](#)]
5. Collins, A.S.; Clark, C.; Plavsa, D. Peninsular India in Gondwana: The Tectonothermal Evolution of the Southern Granulite Terrain and Its Gondwanan Counterparts. *Gondwana Res.* **2014**, *25*, 190–203. [[CrossRef](#)]
6. Santosh, M.; Maruyama, S.; Sato, K. Anatomy of a Cambrian Suture in Gondwana: Pacific-Type Orogeny in Southern India? *Gondwana Res.* **2009**, *16*, 321–341. [[CrossRef](#)]
7. Bhaskar, R.Y.J.; Vijaya, K.T.; Dayal, A.M.; Janardhan, A.S. Sm-Nd Model Age Evidence for Temporally Distinct Precambrian Crustal Blocks across the Cauvery Shear Zone, Southern India. *ISMAS Silver Jubil. Symp. Mass Spectrom.* **2003**, *34*, 661–667.
8. Raith, M.M.; Srikantappa, C.; Buhl, D.; Koehler, H. The Nilgiri Enderbites, South India: Nature and Age Constraints on Protolith Formation, High-Grade Metamorphism and Cooling History. *Precambrian Res.* **1999**, *98*, 129–150. [[CrossRef](#)]
9. Ghosh, J.G.; de Wit, M.J.; Zartman, R.E. Age and Tectonic Evolution of Neoproterozoic Ductile Shear Zones in the Southern Granulite Terrain of India, with Implications for Gondwana Studies. *Tectonics* **2004**, *23*. [[CrossRef](#)]
10. Collins, A.S.; Clark, C.; Sajeev, K.; Santosh, M.; Kelsey, D.E.; Hand, M. Passage through India: The Mozambique Ocean Suture, High-Pressure Granulites and the Palghat-Cauvery Shear Zone System. *Terra Nova* **2007**, *19*, 141–147. [[CrossRef](#)]
11. Chadwick, B.; Vasudev, V.N.; Hegde, G.V. The Dharwar Craton, Southern India, Interpreted as the Result of Late Archaean Oblique Convergence. *Precambrian Res.* **2000**, *99*, 91–111. [[CrossRef](#)]
12. Jayananda, M.; Moyen, J.-F.; Martin, H.; Peucat, J.-J.; Auvray, B.; Mahabaleswar, B. Late Archaean (2550–2520 Ma) Juvenile Magmatism in the Eastern Dharwar Craton, Southern India: Constraints from Geochronology, Nd-Sr Isotopes and Whole Rock Geochemistry. *Precambrian Res.* **2000**, *99*, 225–254. [[CrossRef](#)]
13. Chetty, T.R.K.; Bhaskar Rao, Y.J. The Cauvery Shear Zone, Southern Granulite Terrain, India: A Crustal-Scale Flower Structure. *Gondwana Res.* **2006**, *10*, 77–85. [[CrossRef](#)]
14. Clark, C.; Collins, A.S.; Timms, N.E.; Kinny, P.D.; Chetty, T.R.K.; Santosh, M. SHRIMP U-Pb Age Constraints on Magmatism and High-Grade Metamorphism in the Salem Block, Southern India. *Gondwana Res.* **2009**, *16*, 27–36. [[CrossRef](#)]
15. Samuel, V.O.; Santosh, M.; Liu, S.; Wang, W.; Sajeev, K. Neoproterozoic Continental Growth through Arc Magmatism in the Nilgiri Block, Southern India. *Precambrian Res.* **2014**, *245*, 146–173. [[CrossRef](#)]

16. Samuel, V.O.; Kwon, S.; Santosh, M.; Sajeev, K. Garnet Pyroxenite from Nilgiri Block, Southern India: Vestiges of a Neoproterozoic Volcanic Arc. *Lithos* **2018**, *310–311*, 120–135. [[CrossRef](#)]
17. Tomson, J.K.; Bhaskar Rao, Y.J.; Vijaya Kumar, T.; Choudhary, A.K. Geochemistry and Neodymium Model Ages of Precambrian Charnockites, Southern Granulite Terrain, India: Constraints on Terrain Assembly. *Precambrian Res.* **2013**, *227*, 295–315. [[CrossRef](#)]
18. Srinivasan, V.; Rajeshdurai, P. The Suruli Shear Zone and Regional Scale Folding Pattern in Madurai Block of Southern Granulite Terrain, South India. *J. Earth Syst. Sci.* **2010**, *119*, 147–160. [[CrossRef](#)]
19. Brandt, S.; Schenk, V.; Raith, M.M.; Appel, P.; Gerdes, A.; Srikantappa, C. Late Neoproterozoic P-T Evolution of HP-UHT Granulites from the Palni Hills (South India): New Constraints from Phase Diagram Modelling, LA-ICP-MS Zircon Dating and in-Situ EMP Monazite Dating. *J. Petrol.* **2011**, *52*, 1813–1856. [[CrossRef](#)]
20. Tiwari, A.K.; Sarkar, T. P-T-t Evolution of Sapphirine-Bearing Semipelitic Granulites from Vadkampatti in Eastern Madurai Domain, Southern India: Insights from Petrography, Pseudosection Modelling and in-Situ Monazite Geochronology. *Precambrian Res.* **2020**, *348*, 105866. [[CrossRef](#)]
21. Dev, J.A.; Tomson, J.K.; Sorcar, N.; Anto Francis, K. Timing of UHT Metamorphism and Cooling in South Indian Granulites: New P-T-t Results from a Sapphirine Granulite. *Precambrian Res.* **2022**, *371*, 106582. [[CrossRef](#)]
22. Dev, J.A.; Tomson, J.K.; Sorcar, N.; Nandakumar, V. Combined U-Pb/Hf Isotopic Studies and Phase Equilibrium Modelling of HT-UHT Metapelites from Kambam Ultrahigh-Temperature Belt, South India: Constraints on Tectonothermal History of the Terrane. *Lithos* **2021**, *406–407*, 106531. [[CrossRef](#)]
23. Dev, J.A.; Sorcar, N.; Mukherjee, S.; Tomson, J.K. Phase Equilibrium Modelling and Zircon-Monazite Geochronology of HT-UHT Granulites from Kambam Ultrahigh-Temperature Belt, South India. *Int. Geol. Rev.* **2022**, 1–19. [[CrossRef](#)]
24. Drury, S.A.; Harris, N.B.W.; Holt, R.W.; Reeves-Smith, G.J.; Wightman, R.T. Precambrian Tectonics and Crustal Evolution in South India. *J. Geol.* **1984**, *92*, 3–20. [[CrossRef](#)]
25. Rajesh, H.M.; Santosh, M.; Yoshida, M. Dextral Pan-African Shear Along the Southwestern Edge of the Achankovil Shear Belt, South India: Constraints on Gondwana Reconstructions: A Discussion. *J. Geol.* **1998**, *106*, 105–114. [[CrossRef](#)]
26. Cenki, B.; Braun, I.; Bröcker, M. Evolution of the Continental Crust in the Kerala Khondalite Belt, Southernmost India: Evidence from Nd Isotope Mapping, U-Pb and Rb-Sr Geochronology. *Precambrian Res.* **2004**, *134*, 275–292. [[CrossRef](#)]
27. Cenki, B.; Kriegsman, L.M.; Braun, I. Melt-Producing and Melt-Consuming Reactions in the Achankovil Cordierite Gneisses, South India. *J. Metamorph. Geol.* **2002**, *20*, 543–561. [[CrossRef](#)]
28. Bartlett, J.M.; Dougherty-Page, J.S.; Harris, N.B.W.; Hawkesworth, C.J.; Santosh, M. The Application of Single Zircon Evaporation and Model Nd Ages to the Interpretation of Polymetamorphic Terrains: An Example from the Proterozoic Mobile Belt of South India. *Contrib. Mineral. Petrol.* **1988**, *131*, 181–195. [[CrossRef](#)]
29. Collins, A.S.; Santosh, M.; Braun, I.; Clark, C. Age and Sedimentary Provenance of the Southern Granulites, South India: U-Th-Pb SHRIMP Secondary Ion Mass Spectrometry. *Precambrian Res.* **2007**, *155*, 125–138. [[CrossRef](#)]
30. Santosh, M.; Hu, C.N.; He, X.F.; Li, S.S.; Tsunogae, T.; Shaji, E.; Indu, G. Neoproterozoic Arc Magmatism in the Southern Madurai Block, India: Subduction, Relamination, Continental Outbuilding, and the Growth of Gondwana. *Gondwana Res.* **2017**, *45*, 1–42. [[CrossRef](#)]
31. Braun, I.; Kriegsman, L.M. Proterozoic Crustal Evolution of Southernmost India and Sri Lanka. *Geol. Soc. Spec. Publ.* **2003**, *206*, 169–202. [[CrossRef](#)]
32. Ravindra Kumar, G.R.; Sreejith, C. Petrology and Geochemistry of Charnockites (Felsic Ortho-Granulites) from the Kerala Khondalite Belt, Southern India: Evidence for Intra-Crustal Melting, Magmatic Differentiation and Episodic Crustal Growth. *Lithos* **2016**, *262*, 334–354. [[CrossRef](#)]
33. Harris, N.B.W.; Santosh, M.; Taylor, P.N.; Santosh, M.; Taylor, P.N. Crustal Evolution in South India: Constraints from Nd Isotopes. *J. Geol.* **1994**, *102*, 139–150. [[CrossRef](#)]
34. Kröner, A.; Santosh, M.; Hegner, E.; Shaji, E.; Geng, H.; Wong, J.; Xie, H.; Wan, Y.; Shang, C.K.; Liu, D.; et al. Palaeoproterozoic Ancestry of Pan-African High-Grade Granitoids in Southernmost India: Implications for Gondwana Reconstructions. *Gondwana Res.* **2015**, *27*, 1–37. [[CrossRef](#)]
35. Johnson, T.E.; Clark, C.; Taylor, R.J.M.; Santosh, M.; Collins, A.S. Prograde and Retrograde Growth of Monazite in Migmatites: An Example from the Nagercoil Block, Southern India. *Geosci. Front.* **2015**, *6*, 373–387. [[CrossRef](#)]
36. Clark, C.; Collins, A.S.; Taylor, R.J.M.; Hand, M. Isotopic Systematics of Zircon Indicate an African Affinity for the Rocks of Southernmost India. *Sci. Rep.* **2020**, *10*, 5421. [[CrossRef](#)] [[PubMed](#)]
37. Gao, P.; Santosh, M.; Yang, C.X.; Kwon, S.; Ramkumar, M. High Ba-Sr Adakitic Charnockite Suite from the Nagercoil Block, Southern India: Vestiges of Paleoproterozoic Arc and Implications for Columbia to Gondwana. *Geosci. Front.* **2021**, *12*, 101126. [[CrossRef](#)]
38. Santosh, M.; Tagawa, M.; Yokoyama, K.; Collins, A.S. U-Pb Electron Probe Geochronology of the Nagercoil Granulites, Southern India: Implications for Gondwana Amalgamation. *J. Asian Earth Sci.* **2006**, *28*, 63–80. [[CrossRef](#)]
39. Janoušek, V.; Farrow, C.M.; Erban, V. Interpretation of Whole-Rock Geochemical Data in Igneous Geochemistry: Introducing Geochemical Data Toolkit (GCDkit). *J. Petrol.* **2006**, *47*, 1255–1259. [[CrossRef](#)]
40. Anders, E.; Grevesse, N. Abundances of the Elements: Meteoritic and Solar. *Geochim. Cosmochim. Acta* **1989**, *53*, 197–214. [[CrossRef](#)]

41. Sun, S.S.; McDonough, W.F. Chemical and Isotopic Systematics of Oceanic Basalts: Implications for Mantle Composition and Processes. *Geol. Soc. Lond. Spec. Publ.* **1989**, *42*, 313–345. [[CrossRef](#)]
42. Cox, K.G.; Bell, J.D.; Pankhurst, R.J. *The Interpretation of Igneous Rocks*; Springer: Berlin/Heidelberg, Germany, 1979.
43. Irvine, T.N.; Baragar, W.R.A. A Guide to the Chemical Classification of the Common Volcanic Rocks. *Can. J. Earth Sci.* **1971**, *8*, 523–548. [[CrossRef](#)]
44. Wedenbeck, M.; Alle, P.; Griffin, W.L.; Meer, M.; Oberli, F.; von Quadt, A.; Roddick, J.C.; Spiegel, W. Three Natural Zircon Standards for U-Th-Pb, Lu-Hf, Trace Element and REE Analyses. *Geostand. Newsl.* **1995**, *19*, 1–23. [[CrossRef](#)]
45. Sláma, J.; Košler, J.; Condon, D.J.; Crowley, J.L.; Gerdes, A.; Hanchar, J.M.; Horstwood, M.S.A.; Morris, G.A.; Nasdala, L.; Norberg, N.; et al. Plešovice Zircon—A New Natural Reference Material for U-Pb and Hf Isotopic Microanalysis. *Chem. Geol.* **2008**, *249*, 1–35. [[CrossRef](#)]
46. Santos, M.M.; Lana, C.; Scholz, R.; Buick, I.; Schmitz, M.D.; Kamo, S.L.; Gerdes, A.; Corfu, F.; Tapster, S.; Lancaster, P.; et al. A New Appraisal of Sri Lankan BB Zircon as a Reference Material for LA-ICP-MS U-Pb Geochronology and Lu-Hf Isotope Tracing. *Geostand. Geoanal. Res.* **2017**, *41*, 335–358. [[CrossRef](#)]
47. Paton, C.; Hellstrom, J.; Paul, B.; Woodhead, J.; Hergt, J. Iolite: Freeware for the Visualisation and Processing of Mass Spectrometric Data. *J. Anal. At. Spectrom.* **2011**, *26*, 2508–2518. [[CrossRef](#)]
48. Ludwig, K.R. Isoplot Version 4.15: A Geochronological Toolkit for Microsoft Excel. In *Berkeley Geochronology Center Special Publication*; Berkeley Geochronology Center: Berkeley, CA, USA, 2011; Available online: <https://www.bgc.org/isoplot> (accessed on 21 November 2022).
49. Pearce, N.J.G.; Perkins, W.T.; Westgate, J.A.; Gorton, M.P.; Jackson, S.E.; Neal, C.R.; Chenery, S.P. A Compilation of New and Published Major and Trace Element Data for NIST SRM 610 and NIST SRM 612 Glass Reference Materials. *J. Geostand. Geoanalysis* **1997**, *21*, 115–144. [[CrossRef](#)]
50. Ferry, J.M.; Watson, E.B. New Thermodynamic Models and Revised Calibrations for the Ti-in-Zircon and Zr-in-Rutile Thermometers. *Contrib. Mineral. Petrol.* **2007**, *154*, 429–437. [[CrossRef](#)]
51. Scherer, E.; Münker, C.; Mezger, K. Calibration of the Lutetium-Hafnium Clock. *Science* **2001**, *293*, 683–687. [[CrossRef](#)]
52. Blichert-Toft, J.; Albarkde, F. EPSL The Lu-Hf Isotope Geochemistry of Chondrites and the Evolution of the Mantle-Crust System. *Earth Planet. Sci. Lett.* **1997**, *148*, 243–258. [[CrossRef](#)]
53. Nowell, G.M.; Kempton, P.D.; Noble, S.R.; Fitton, J.G.; Saunders, A.D.; Mahoney, J.J.; Taylor, R.N. High Precision Hf Isotope Measurements of MORB and OIB by Thermal Ionisation Mass Spectrometry: Insights into the Depleted Mantle. *Chem. Geol.* **1998**, *149*, 211–233. [[CrossRef](#)]
54. Griffin, W.L.; Pearson, N.J.; Belousova, E.; Jackson, S.E.; van Acherbergh, E.; O’reilly, S.Y.; Shee, S.R. The Hf Isotope Composition of Cratonic Mantle: LAM-MC-ICPMS Analysis of Zircon Megacrysts in Kimberlites. *Geochim. Cosmochim. Acta* **2000**, *64*, 133–147. [[CrossRef](#)]
55. Deevsalar, R.; Shinjo, R.; Ghaderi, M.; Murata, M.; Hoskin, P.W.O.; Oshiro, S.; Wang, K.L.; Lee, H.Y.; Neill, I. Mesozoic–Cenozoic Mafic Magmatism in Sanandaj–Sirjan Zone, Zagros Orogen (Western Iran): Geochemical and Isotopic Inferences from Middle Jurassic and Late Eocene Gabbros. *Lithos* **2017**, *284–285*, 588–607. [[CrossRef](#)]
56. Yu, B.; Santosh, M.; Wang, M.X.; Yang, C.X. Paleoproterozoic Emplacement and Cambrian Ultrahigh-Temperature Metamorphism of a Layered Magmatic Intrusion from the Central Madurai Block, Southern India: From Columbia to Gondwana. *Geosci. Front.* **2022**, *13*, 101260. [[CrossRef](#)]
57. Hollocher, K.; Robinson, P.; Walsh, E.; Roberts, D. Geochemistry of Amphibolite-Facies Volcanics and Gabbros of the Støren Nappe in Extensions West and Southwest of Trondheim, Western Gneiss Region, Norway: A Key to Correlations and Paleotectonic Settings. *Am. J. Sci.* **2012**, *312*, 357–416. [[CrossRef](#)]
58. Miiller, D.; Rock, S.; Groves, D.I. Mineralogy Geochemical Discrimination between Shoshonitic and Potassic Volcanic Rocks in Different Tectonic Settings: A Pilot Study. *Mineral. Petrol.* **1992**, *46*, 259–289. [[CrossRef](#)]
59. Yang, Q.Y.; Ganguly, S.; Shaji, E.; Dong, Y.; Nanda-Kumar, V. Extensional Collapse of the Gondwana Orogen: Evidence from Cambrian Mafic Magmatism in the Trivandrum Block, Southern India. *Geosci. Front.* **2019**, *10*, 263–284. [[CrossRef](#)]
60. Smith, E.I.; Sánchez, A.; Walker, J.D.; Wang, K. Geochemistry of Mafic Magmas in the Hurricane Volcanic Field, Utah: Implications for Small- and Large-Scale Chemical Variability of the Lithospheric Mantle. *J. Geol.* **1999**, *107*, 433–448. [[CrossRef](#)]
61. Menzies, M.A.; Kyle, P.R.; Jones, M.; Ingram, G. Enriched and Depleted Source Components for Tholeiitic and Alkaline Lavas from Zuni-Bandera, New Mexico: Inferences about Intraplate Processes and Stratified Lithosphere. *J. Geophys. Res.* **1991**, *96*, 13645–13671. [[CrossRef](#)]
62. Depaolo, D.J.; Daley, E.E.; Depaolo, D.J. Neodymium Isotopes in Basalts of the Southwest Basin and Range and Lithospheric Thinning during Continental Extension. *Chem. Geol.* **2000**, *169*, 157–185. [[CrossRef](#)]
63. Pearce, J.A. Geochemical Fingerprinting of Oceanic Basalts with Applications to Ophiolite Classification and the Search for Archean Oceanic Crust. *Lithos* **2008**, *100*, 14–48. [[CrossRef](#)]
64. Cui, X.; Sun, M.; Zhao, G.; Zhang, Y. Origin of Permian Mafic Intrusions in Southern Chinese Altai, Central Asian Orogenic Belt: A Post-Collisional Extension System Triggered by Slab Break-Off. *Lithos* **2021**, *390–391*, 106112. [[CrossRef](#)]
65. Carlson, R.W.; Hart, W.K. Flood Basalt Volcanism in the Northwestern United States. In *Petrology and Structural Geology*; Springer: Berlin/Heidelberg, Germany, 1988; Volume 360, pp. 35–61.

66. Gündüz, M.; Asan, K. PetroGram: An Excel-Based Petrology Program for Modeling of Magmatic Processes. *Geosci. Front.* **2021**, *12*, 81–92. [[CrossRef](#)]
67. McDonough, W.F. Constraints on the Composition of the Continental Lithospheric Mantle. *Earth Planet. Sci. Lett.* **1990**, *101*, 1–18. [[CrossRef](#)]
68. Frey, F.A. Rare Earth Element Abundances in Upper Mantle Rocks. *Dev. Geochem.* **1984**, *2*, 153–203.
69. McKenzie, D.; Bickle, M.J. The Volume and Composition of Melt Generated by Extension of the Lithosphere. *J. Petrol.* **1988**, *29*, 625–679. [[CrossRef](#)]
70. Corfu, F.; Hanchar, J.M.; Hoskin, P.W.; Kinny, P. Atlas of Zircon Textures. *Rev. Mineral. Geochem.* **2003**, *53*, 469–500. [[CrossRef](#)]
71. Kirkland, C.L.; Smithies, R.H.; Taylor, R.J.M.; Evans, N.; McDonald, B. Zircon Th/U Ratios in Magmatic Environments. *Lithos* **2015**, *212–215*, 397–414. [[CrossRef](#)]
72. Hoskin, P.W.O.; Schaltegger, U. The Composition of Zircon and Igneous and Metamorphic Petrogenesis. *Rev. Mineral. Geochem.* **2003**, *53*, 27–62. [[CrossRef](#)]
73. Rubatto, D.; Hermann, J. Zircon Formation during Fluid Circulation in Eclogites (Monviso, Western Alps): Implications for Zr and Hf Budget in Subduction Zones. *Geochim. Cosmochim. Acta* **2003**, *67*, 2173–2187. [[CrossRef](#)]
74. Fu, B.; Page, F.Z.; Cavosie, A.J.; Fournelle, J.; Kita, N.T.; Lackey, J.S.; Wilde, S.A.; Valley, J.W. Ti-in-Zircon Thermometry: Applications and Limitations. *Contrib. Mineral. Petrol.* **2008**, *156*, 197–215. [[CrossRef](#)]
75. Kohn, M.J.; Engi, M.; Lanari, P. Petrochronology. *Methods Appl. Mineral. Soc. Am. Rev. Mineral. Geochem.* **2017**, *83*, 575.
76. Grimes, C.B.; John, B.E.; Kelemen, P.B.; Mazdab, F.K.; Wooden, J.L.; Cheadle, M.J.; Hanghøj, K.; Schwartz, J.J. Trace Element Chemistry of Zircons from Oceanic Crust: A Method for Distinguishing Detrital Zircon Provenance. *Geology* **2007**, *35*, 643–646. [[CrossRef](#)]
77. Kröner, A.; Rojas-Agramonte, Y.; Kehelpanala, K.V.W.; Zack, T.; Hegner, E.; Geng, H.Y.; Wong, J.; Barth, M. Age, Nd-Hf Isotopes, and Geochemistry of the Vijayan Complex of Eastern and Southern Sri Lanka: A Grenville-Age Magmatic Arc of Unknown Derivation. *Precambrian Res.* **2013**, *234*, 288–321. [[CrossRef](#)]
78. Plavsa, D.; Collins, A.S.; Foden, J.F.; Kropinski, L.; Santosh, M.; Chetty, T.R.K.; Clark, C. Delineating Crustal Domains in Peninsular India: Age and Chemistry of Orthopyroxene-Bearing Felsic Gneisses in the Madurai Block. *Precambrian Res.* **2012**, *198–199*, 77–93. [[CrossRef](#)]
79. Bhattacharya, S.; Santosh, M.; Zhang, Z.; Huang, H.; Banerjee, A.; George, P.M.; Sajeev, K. Imprints of Archean to Neoproterozoic Crustal Processes in the Madurai Block, Southern India. *J. Asian Earth Sci.* **2014**, *88*, 1–10. [[CrossRef](#)]
80. George, P.M.; Santosh, M.; Chen, N.; Nandakumar, V.; Itaya, T.; Sonali, M.K.; Smruti, R.P.; Sajeev, K. Cryogenian Magmatism and Crustal Reworking in the Southern Granulite Terrane, India. *Int. Geol. Rev.* **2015**, *57*, 112–133. [[CrossRef](#)]
81. Plavsa, D.; Collins, A.S.; Foden, J.D.; Clark, C. The evolution of a Gondwanan collisional orogen: A structural and geochronological appraisal from the Southern Granulite Terrane, South India. *Tectonics*. **2015**, *34*, 820–857. [[CrossRef](#)]
82. Kooijman, E.; Upadhyay, D.; Mezger, K.; Raith, M.M.; Berndt, J.; Srikantappa, C. Response of the U-Pb Chronometer and Trace Elements in Zircon to Ultrahigh-Temperature Metamorphism: The Kadavur Anorthosite Complex, Southern India. *Chem. Geol.* **2011**, *290*, 177–188. [[CrossRef](#)]
83. Santosh, M.; Tsunogae, T.; Malaviarachchi, S.P.K.; Zhang, Z.; Ding, H.; Tang, L.; Dharmapriya, P.L. Neoproterozoic Crustal Evolution in Sri Lanka: Insights from Petrologic, Geochemical and Zircon U-Pb and Lu-Hf Isotopic Data and Implications for Gondwana Assembly. *Precambrian Res.* **2014**, *255*, 1–29. [[CrossRef](#)]
84. Tewari, S.; Prakash, D.; Yadav, M.K.; Yadav, R. Petrology and Isotopic Evolution of Granulites from Central Madurai Block (Southern India): Reference to Ediacaran Crustal Evolution. *Int. Geol. Rev.* **2018**, *60*, 1792–1815. [[CrossRef](#)]
85. Shimizu, H.; Tsunogae, T.; Santosh, M. Spinel + Quartz Assemblage in Granulites from the Achankovil Shear Zone, Southern India: Implications for Ultrahigh-Temperature Metamorphism. *J. Asian Earth Sci.* **2009**, *36*, 209–222. [[CrossRef](#)]
86. Harley, S.L.; Nandakumar, V. New Evidence for Palaeoproterozoic High Grade Metamorphism in the Trivandrum Block, Southern India. *Precambrian Res.* **2016**, *280*, 120–138. [[CrossRef](#)]
87. Sorcar, N.; Joshi, K.B.; Oliveira, E.P.; Tomson, J.K.; Nandakumar, V. Characterization of Partial Melting Events in Garnet-Cordierite Gneiss from the Kerala Khondalite Belt, India. *Geosci. Front.* **2020**, *11*, 597–611. [[CrossRef](#)]
88. Spreitzer, S.K.; Walters, J.B.; Cruz-Urbe, A.; Williams, M.L.; Yates, M.G.; Jercinovic, M.J.; Grew, E.S.; Carson, C.J. Monazite Petrochronology of Polymetamorphic Granulite-Facies Rocks of the Larsemann Hills, Prydz Bay, East Antarctica. *J. Metamorph. Geol.* **2021**, *39*, 1205–1228. [[CrossRef](#)]
89. Dharmapriya, P.L.; Kriegsman, L.M.; Malaviarachchi, S.P.K. Spatial Distribution of Ultrahigh-Temperature Granulites of the Highland Complex of Sri Lanka: Lowermost Continental Crust above an Ultrahot Palaeo-Moho. *Lithos* **2021**, *404–405*, 106484. [[CrossRef](#)]
90. Raith, M.M.; Rakotondrazafy, R.; Sengupta, P. Petrology of Corundum-Spinel-Sapphirine-Anorthite Rocks (Sakenites) from the Type Locality in Southern Madagascar. *J. Metamorph. Geol.* **2008**, *26*, 647–667. [[CrossRef](#)]
91. Kelsey, D.E.; Hand, M. On Ultrahigh Temperature Crustal Metamorphism: Phase Equilibria, Trace Element Thermometry, Bulk Composition, Heat Sources, Timescales and Tectonic Settings. *Geosci. Front.* **2015**, *6*, 311–356. [[CrossRef](#)]
92. Nandakumar, V.; Harley, S.L. A Reappraisal of the Pressure-Temperature Path of Granulites from the Kerala Khondalite Belt, Southern India. *J. Geol.* **2000**, *108*, 687–703. [[CrossRef](#)]

93. Nandakumar, V.; Harley, S.L. Geochemical Signatures of Mid-Crustal Melting Processes and Heat Production in a Hot Orogen: The Kerala Khondalite Belt, Southern India. *Lithos* **2019**, *324–325*, 479–500. [[CrossRef](#)]
94. Klaver, M.; de Roever, E.W.F.; Thijssen, A.C.D.; Bleeker, W.; Söderlund, U.; Chamberlain, K.; Ernst, R.; Berndt, J.; Zeh, A. Mafic Magmatism in the Bakhuis Granulite Belt (Western Suriname): Relationship with Charnockite Magmatism and UHT Metamorphism. *GFF* **2016**, *138*, 203–218. [[CrossRef](#)]
95. Guo, J.H.; Peng, P.; Chen, Y.; Jiao, S.J.; Windley, B.F. UHT Sapphirine Granulite Metamorphism at 1.93–1.92Ga Caused by Gabbro Intrusions: Implications for Tectonic Evolution of the Northern Margin of the North China Craton. *Precambrian Res.* **2012**, *222–223*, 124–142. [[CrossRef](#)]
96. Wang, B.; Wei, C.-J.; Tian, W.; Fu, B.; Wei, C. UHT Metamorphism Peaking above 1100 °C with Slow Cooling: Insights from Pelitic Granulites in the Jining Complex, North China Craton. *J. Petrol.* **2020**, *61*, ega070. [[CrossRef](#)]
97. Della Giustina, M.E.S.; Pimentel, M.M.; Ferreira Filho, C.F.; de Hollanda, M.H.B.M. Dating Coeval Mafic Magmatism and Ultrahigh Temperature Metamorphism in the Anápolis-Itaúçu Complex, Central Brazil. *Lithos* **2011**, *124*, 82–102. [[CrossRef](#)]
98. Takamura, Y.; Tsunogae, T.; Santosh, M.; Malaviarachchi, S.P.K.; Tsutsumi, Y. Petrology and Zircon U-Pb Geochronology of Metagabbro from the Highland Complex, Sri Lanka: Implications for the Correlation of Gondwana Suture Zones. *J. Asian Earth Sci.* **2015**, *113*, 826–841. [[CrossRef](#)]
99. Takamura, Y.; Tsunogae, T.; Tsutsumi, Y. U-Pb Geochronology and REE Geochemistry of Zircons in Mafic Granulites from the Lützow-Holm Complex, East Antarctica: Implications for the Timing and P-T Path of Post-Peak Exhumation and Antarctica–Sri Lanka Correlation. *Precambrian Res.* **2020**, *348*, 105850. [[CrossRef](#)]